Award Accounts
The Chemical Society of Japan Award for Creative Work for 2007

Looking at Molecular Orbitals in Three-Dimensional Form: From Dream to Reality

Masahiko Takahashi

Institute of Multidisciplinary Research for Advanced Materials, Tohoku University, Sendai 980-8577

Received November 17, 2008; E-mail: masahiko@tagen.tohoku.ac.jp

Over the last four decades an experimental method has been developed for looking at electron orbitals in momentum space. The method, called electron momentum spectroscopy (EMS), is based on the electron-impact ionizing reaction near the Bethe ridge at incident electron energies of the order of 1 keV or higher. This account reviews frontiers of the field, involving the first approach to molecular frame EMS that enables one to look at molecular orbitals in three-dimensional form.

1. Introduction

Allow me to begin this account by reminding ourselves about the basic physics of electron inelastic collisions. An atom or molecule may be raised from an initial state to another state of higher electronic energy in a collision with an incident electron whose kinetic energy is sufficiently high. The resultant inelastically scattered electron with a lower kinetic energy emerges traveling in a direction. The time-independent probability for the occurrence of such a particular collision process is represented by the corresponding double differential cross section. In the framework of the first-order Born approximation,[1,2] which assumes the effect of the scattering potential is small so that the interaction between the incident electron and the target atom or molecule can be treated as a perturbation and keeps only the first term of the Born expansion of the scattering amplitude, the cross section $d^2\sigma/dEd\Omega_1$ is given by the Bethe–Born formula,[3,4]

$$\frac{d^2\sigma}{dEd\Omega_1} = \frac{p_1}{p_0 K^2} \frac{4}{E} \frac{df(K,E)}{dE} \tag{1}$$

with

$$\frac{df(K,E)}{dE} = \sum_f \frac{E_f}{K^2} \left| \langle \Psi_f | \sum_{j=1}^{N} \exp(i\boldsymbol{K} \cdot \boldsymbol{r}_j) | \Psi_i \rangle \right|^2 \delta(E_f - E) \tag{2}$$

Here, E ($=E_0 - E_1$) and $\boldsymbol{K}$ ($=\boldsymbol{p}_0 - \boldsymbol{p}_1$) are the energy and momentum transferred to the target atom or molecule from the incident electron. E_0 (or E_1) and $\boldsymbol{p}_0$ (or $\boldsymbol{p}_1$) are the kinetic energy and momentum of the incident (or inelastically scattered) electron. $d\Omega_1$ corresponds to the solid angle of the inelastically scattered electron detected. Ψ_i and Ψ_f are the N-electron wave functions of the initial and final target states, respectively. $\boldsymbol{r}_j$ is the position of the j-th electron. $df(K,E)/dE$ is a quantity called the generalized oscillator strength (GOS).[2,3] The GOS at

any K value can be put on an absolute scale independently by using the Bethe sum rule,[3]

$$\int \frac{df(K,E)}{dE} dE = N \tag{3}$$

An example of the GOS is shown in Figure 1, where the GOS of He obtained by angle-resolved electron energy loss spectroscopy (EELS)[5] is plotted as a function of energy loss E and momentum transfer K. This kind of three-dimensional plot of the GOS is often called the Bethe surface.[3] Note that the same Bethe surface can be obtained by using other projectiles such as X-rays instead of electrons. In Figure 1 we can see some commonly noted features of the Bethe surface. For instance, at small momentum transfers or in the forward scattering direction of the electron projectile we have the dipole
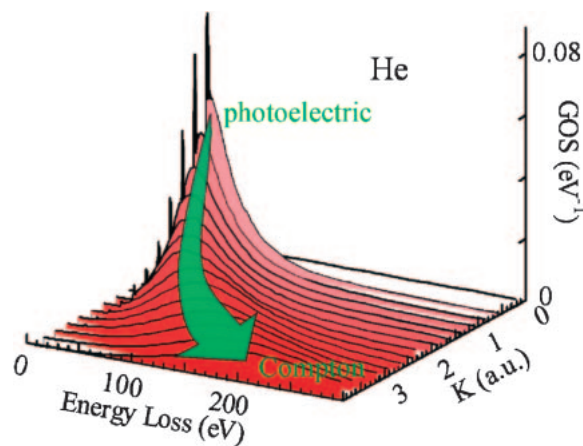
Figure 1. Bethe surface of He, which was obtained at an incident electron energy of 3.0 keV using an angle-resolved EELS spectrometer [Ref. 5].

regime in which excitation of the target is very similar to photoabsorption. In these cases the momentum transfer unit vector ($K/|K|$) and the electric vector of light play the same role, as can be seen in the following equation.

$$\frac{df(K,E)}{dE} = \sum_f \frac{E_f}{K^2} \left| \langle \Psi_f | \sum_{j=1}^{N} (1 + iK \cdot r_j + \cdots) | \Psi_i \rangle \right|^2 \delta(E_f - E)$$

$$\approx \sum_f E_f \left| \langle \Psi_f | \sum_{j=1}^{N} \left(\frac{K}{K} \cdot r_j \right) | \Psi_i \rangle \right|^2 \delta(E_f - E) \quad (4)$$

In other words, the GOS converges to the optical oscillator strength, $df_0(E)/dE$, as the momentum transfer approaches zero,[6]

$$\lim_{K \to 0} \frac{df(K,E)}{dE} = \frac{df_0(E)}{dE} \quad (5)$$

More interestingly, the global feature of the Bethe surface can be seen by turning our eyes upon the momentum transfer dependence of the GOS; as the momentum transfer increases, the continuum part of the GOS spectrum, which corresponds to ionization transitions, moves towards higher energy loss, whilst the peak width becomes broader. The diagonal ridge running through the Bethe surface is called the Bethe ridge, and its high-energy limit is known as Compton scattering.[7] Electron momentum spectroscopy (EMS) that will be discussed in this account is a kinematically-complete electron-impact ionization experiment under such high-energy Bethe ridge conditions.

Historically, the use of electron Compton scattering[7] to investigate the electronic structure of matter can be traced back to 1938. Between 1938 and 1941 Hughes et al.[8–11] reported a series of papers on electron Compton scattering, showing that the Doppler broadening of inelastically scattered electrons, the Compton profile, directly provides information about the momentum distribution of the electrons in matter. This experiment is completely analogous to the better known X-ray Compton scattering experiment, except that incident X-rays are replaced by high-energy electrons. Since, in quantum mechanics, the position- and momentum-space wave functions of any physical system are related by the Dirac–Fourier transform, information obtained from Compton scattering experiments is complementary to that obtained from other standard techniques, such as X-ray diffraction, which provide information about spatial distributions of the target electrons.

The theory of EMS type experiments was proposed independently by McCarthy[12,13] and by Smirnov and Neudatchin,[14,15] who were nuclear structure theorists working on the theory of the (p,2p) reaction. In the reaction, a proton ejected from the nucleus due to high-energy proton bombardment as well as the inelastically scattered proton is observed. Likewise, EMS is based on the (e,2e) reaction[16] in which an electron ejected from matter due to electron impact ionization as well as the inelastically scattered electron is observed. Note that the importance of such observations lies in the exciting possibility of measuring Compton profiles associated with target electrons in different energy levels separately; one becomes capable to look at individual electron orbitals in momentum space. Thus EMS can be seen as an evolutionary development from the conventional Compton scattering experiments. From consideration of the nature of the Dirac–Fourier

transform the EMS method is fully expected to be particularly sensitive to the behavior of the outer, loosely bound valence electrons that are of central importance in chemical properties such as bonding, chemical reactivity, and molecular recognition. This is in a sharp contrast with the fact that theoretical wave functions generated by using the variational principle are governed principally by tightly bound electrons at the inner regions near the nuclei.

Once the feasibility of EMS experiments was demonstrated in 1969 by Amaldi et al.[17] and later by Camilloni et al.[18] and Weigold et al.,[19] chemists also became interested and a large number of EMS measurements were performed for a wide variety of targets ranging from atoms to molecules of biochemical interest. Various kinds of successful attempts, such as the experimental determination of the atomic hydrogen wave function,[20] stringent testing of ab initio wave functions,[21–24] identification of many-body states and orbital ordering,[25–28] qualification of orbital symmetries,[29,30] Fourier analysis of orbital momentum densities,[31–33] examination of relativistic effects in outer valence orbitals,[34–36] investigation of (e,2e) reactions of atoms in excited states,[37] and the electronic structure study of weakly-bonded compounds,[38] were reported. Developments of multichannel techniques[33,39–44] have promoted the expansion in the range of applications of EMS by improving the sensitivity to probe the inherently small EMS cross section. As well, developments of monochromated electron beam sources[28] have made it possible to apply EMS to larger molecules for which better energy-resolution should be desired. The reader can refer to excellent articles[45–54] for this renaissance of EMS and the literature up until 2000.

The present account is organized to review frontiers of the field after 2000. Emphasis is placed on the new attempts that develop unexploited areas of EMS, opening the door for more detailed studies of bound electron wave functions as well as those of stereodynamics of electron–molecule collisions. I will begin with a brief description of the EMS theory, which some of broad readers in chemistry may not be familiar with, and then introduce the experimental techniques, followed by a review of a selection of recent studies by my group. Finally, a perspective of EMS will be drawn.

2. Theoretical Background

2.1 Kinematics. EMS is an electron-impact ionization experiment in which both the inelastically scattered and ejected electrons are detected in coincidence. The (e,2e) reaction that ionizes the target atom or molecule, M, can be described by

$$M + e_0^-(E_0, p_0)$$
$$\to e_1^-(E_1, p_1) + e_2^-(E_2, p_2) + M^+(E_{recoil}, q) \quad (6)$$
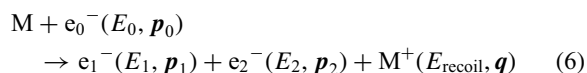
where E_{recoil} and q are the recoil energy and recoil momentum of the residual ion M$^+$. Similarly, the E_j's and p_j's ($j = 0$, 1, and 2) are the kinetic energies and momenta of the incident, inelastically scattered, and ejected electrons, respectively. Here the terms "inelastically scattered" and "ejected" are used for convenience, although the two outgoing electrons are indistinguishable. It is common to assign the indices "1" to the fast "inelastically scattered" electron and "2" to the slow "ejected" electron. The target is considered to be at rest, because its thermal energy and momentum can be neglected in the (e,2e)

M. Takahashi

Bull. Chem. Soc. Jpn. Vol. 82, No. 7 (2009)   753

reaction under consideration. The ion recoil energy E_{recoil} is also negligibly small compared with the ejected electron energy E_2. Hence we have the following conservation laws of momentum and energy:

$$\boldsymbol{q} = \boldsymbol{p}_0 - \boldsymbol{p}_1 - \boldsymbol{p}_2 \qquad (7)$$

and

$$E_{bind} = E_0 - E_1 - E_2 \qquad (8)$$

where E_{bind} is the electron binding energy (also called the ionization energy). Thus the (e,2e) cross section can be measured as a function of $\boldsymbol{q}$ and E_{bind}, because the energy and momentum of the incident electron are known beforehand.

When the (e,2e) reaction takes place so that it is described by the binary encounter approximation,[45,53] which assumes a clean knockout, billiard-like collision between the incident electron and a bound target electron with the residual ion acting as a spectator, the initial momentum of the target electron $\boldsymbol{p}$, before ionization, is equal in magnitude but opposite in sign to the ion recoil momentum $\boldsymbol{q}$:

$$\boldsymbol{p} = -\boldsymbol{q} = \boldsymbol{p}_1 + \boldsymbol{p}_2 - \boldsymbol{p}_0 \qquad (9)$$

A requirement for such clean knockout conditions is that the momentum transfer K ($=|\boldsymbol{p}_0 - \boldsymbol{p}_1|$) is large and all the momentum transferred to the target is absorbed by the ejected electron, as in X-ray Compton scattering.[7] For this reason EMS experiments are usually restricted to be performed near the Bethe ridge,[2,3] which is characterized by

$$|\boldsymbol{K}| = |\boldsymbol{p}_2| \qquad (10)$$

Note that eq 10 is always valid for the collision of two free electrons. Another requirement is that energies of all the incident and outgoing electrons are sufficiently high so that their wave functions can be described by plane waves. The high-energy Bethe ridge conditions fulfil these two requirements, thus making it possible to observe the (e,2e) reaction that most nearly corresponds to a collision of two free electrons with the residual ion acting as a spectator, that is, the so-called binary (e,2e) reaction.

The symmetric noncoplanar geometry is best suited to see the binary (e,2e) reaction that occurs under the high-energy Bethe ridge conditions. The kinematics is illustrated in Figure 2, where the two outgoing electrons having equal energies ($E_1 = E_2$) and making equal polar angles ($\theta_1 = \theta_2 = 45°$) with respect to the incident electron momentum vector are detected in coincidence. The magnitude of the ion recoil momentum q or that of the target electron momentum p is then given by

$$q = p = \left[\left(p_0 - \sqrt{2}p_1 \right)^2 + \left(\sqrt{2}p_1 \sin(\Delta\phi/2) \right)^2 \right]^{1/2} \qquad (11)$$

where $\Delta\phi$ ($=\phi_2 - \phi_1 - \pi$) is the out-of-plane azimuthal angle difference between the two outgoing electrons. Equation 11 tells us that at sufficiently high incident electron energy where $p_0 \approx \sqrt{2}p_1$ the component of $\boldsymbol{q}$ perpendicular to the incident electron momentum vector, $\boldsymbol{q}_\perp$ ($q_\perp = \sqrt{2}p_1 \sin(\Delta\phi/2)$), dominates over the parallel component $\boldsymbol{q}_\parallel$ ($q_\parallel = p_0 - \sqrt{2}p_1$). Thus, basically the symmetric noncoplanar geometry probes $\boldsymbol{q} \approx \boldsymbol{q}_\perp$.

2.2 Differential Cross Section. A full discussion of the scattering theory of EMS can be found in the literature,[45–53] so I
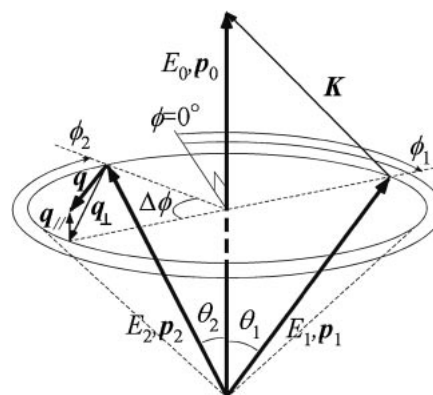
Figure 2. Symmetric noncoplanar geometry for the study of the binary (e,2e) reaction.

do not repeat those details here. Briefly, however, the triple differential cross section (TDCS) for an (e,2e) reaction is given[45,53] by

$$\frac{d^3\sigma}{d\Omega_1 d\Omega_2 dE_1} = (2\pi)^4 \frac{p_1 p_2}{p_0} \sum_{av} |\langle \boldsymbol{p}_1 \boldsymbol{p}_2 \Psi_f | T | \Psi_i \boldsymbol{p}_0 \rangle|^2 \qquad (12)$$

Here T represents the operator that governs the transition from the entrance channel, defined by the incident electron momentum $\boldsymbol{p}_0$ and the initial neutral target state Ψ_i, to the exit channel, defined by the two outgoing electron momenta $\boldsymbol{p}_1$, $\boldsymbol{p}_2$ and the final ion state Ψ_f. $\sum_{av}$ represents an average over the initial degenerate states and a sum over final states that are unresolved in the experiment. For molecular targets $\sum_{av}$ involves the average over orientations Ω of the molecular axes. The T-matrix element $\langle \boldsymbol{p}_1 \boldsymbol{p}_2 \Psi_f | T | \Psi_i \boldsymbol{p}_0 \rangle$ is the ionization amplitude that is the object of theoretical calculations.

The most fundamental approximation made to evaluate the ionization amplitude is the binary encounter approximation[45,53] mentioned above. It assumes that the operator T depends on the coordinates of only the incident and target electrons. By introducing the identity operator $\int d^3p |\boldsymbol{p}\rangle \langle \boldsymbol{p}|$ in the space of the ejected electron, we have

$$\langle \boldsymbol{p}_1 \boldsymbol{p}_2 \Psi_f | T | \Psi_i \boldsymbol{p}_0 \rangle = \int d^3p \langle \boldsymbol{p}_1 \boldsymbol{p}_2 | T | \boldsymbol{p} \boldsymbol{p}_0 \rangle \langle \boldsymbol{p} \Psi_f | \Psi_i \rangle \qquad (13)$$

This equation means that the integrand can be divided into two factors, the collision amplitude $\langle \boldsymbol{p}_1 \boldsymbol{p}_2 | T | \boldsymbol{p} \boldsymbol{p}_0 \rangle$ and the structure factor $\langle \boldsymbol{p} \Psi_f | \Psi_i \rangle$. Note that the collision amplitude can be regarded as a transform that connects the actual ionization amplitude to the structure factor. The simplest transform is given by the first-order Born approximation[1,2] under an assumption that the incident and inelastically scattered electrons are the same:

$$\langle \boldsymbol{p}_1 \boldsymbol{p}_2 | T | \boldsymbol{p} \boldsymbol{p}_0 \rangle = \frac{1}{2\pi^2 |\boldsymbol{p}_0 - \boldsymbol{p}_1|^2} \delta(\boldsymbol{p} + \boldsymbol{q}) \qquad (14)$$

Hence, if the Born approximation were valid, the ionization amplitude is expressed as the product of the collision amplitude and the structure factor:

$$\langle \boldsymbol{p}_1 \boldsymbol{p}_2 \Psi_f | T | \Psi_i \boldsymbol{p}_0 \rangle = \frac{1}{2\pi^2 |\boldsymbol{p}_0 - \boldsymbol{p}_1|^2} \langle \boldsymbol{p} \Psi_f | \Psi_i \rangle \qquad (15)$$

where $\boldsymbol{p}$ is equal in magnitude and opposite in sign to the ion recoil momentum $\boldsymbol{q}$ obtained for the binary (e,2e) reaction (see eq 9). Here is a concrete example to guide our thinking about why the (e,2e) cross section can be directly connected with the target electron momentum density $|\langle \boldsymbol{p}\Psi_\mathrm{f}|\Psi_\mathrm{i}\rangle|^2$.

For predicting the binary (e,2e) reaction, however, the plane wave impulse approximation (PWIA)[48,53,55] has been widely used so far. The PWIA models the binary encounter ionization amplitude in eq 13 as

$$\langle \boldsymbol{p}_1\boldsymbol{p}_2\Psi_\mathrm{f}|T|\Psi_\mathrm{i}\boldsymbol{p}_0\rangle = \int \mathrm{d}^3p\langle \boldsymbol{p}_1\boldsymbol{p}_2|t|\boldsymbol{p}\boldsymbol{p}_0\rangle\langle \boldsymbol{p}\Psi_\mathrm{f}|\Psi_\mathrm{i}\rangle$$
$$= \langle \boldsymbol{p}''|t|\boldsymbol{p}'\rangle\langle \boldsymbol{p}\Psi_\mathrm{f}|\Psi_\mathrm{i}\rangle \qquad (16)$$

where

$$\boldsymbol{p}'' = \frac{1}{2}(\boldsymbol{p}_1 - \boldsymbol{p}_2), \quad \boldsymbol{p}' = \frac{1}{2}(\boldsymbol{p}_0 - \boldsymbol{p}) \qquad (17)$$

This assumes that energies of the continuum electrons are so high that their interaction with the residual ion can be neglected. On the other hand, the electron–electron collision is exactly treated by using the two-electron operator t. The TDCS of the PWIA takes the following form:

$$\frac{\mathrm{d}^3\sigma_\mathrm{PWIA}}{\mathrm{d}\Omega_1\mathrm{d}\Omega_2\mathrm{d}E_1} = (2\pi)^4\frac{p_1p_2}{p_0}f_\mathrm{ee}\sum_\mathrm{av}|\langle \boldsymbol{p}\Psi_\mathrm{f}|\Psi_\mathrm{i}\rangle|^2 \qquad (18)$$

Here the electron–electron collision factor f_ee is given[53,56] by

$$f_\mathrm{ee} = \frac{1}{4\pi^4}\frac{2\pi\eta}{\exp(2\pi\eta) - 1}$$
$$\times \left[\frac{1}{|\boldsymbol{p}_0 - \boldsymbol{p}_1|^4} + \frac{1}{|\boldsymbol{p}_0 - \boldsymbol{p}_2|^4}\right.$$
$$\left. - \frac{1}{|\boldsymbol{p}_0 - \boldsymbol{p}_1|^2}\frac{1}{|\boldsymbol{p}_0 - \boldsymbol{p}_2|^2}\cos\left(\eta\ln\frac{|\boldsymbol{p}_0 - \boldsymbol{p}_1|^2}{|\boldsymbol{p}_0 - \boldsymbol{p}_2|^2}\right)\right] \qquad (19)$$

with

$$\eta = \frac{1}{|\boldsymbol{p}_1 - \boldsymbol{p}_2|} \qquad (20)$$

Figure 3 shows the $\Delta\phi$-angle dependence of f_ee in the symmetric noncoplanar geometry. It is evident that f_ee is essentially constant against the $\Delta\phi$-angle variation over the 0–40° range that experiments usually cover. The flux factor p_1p_2/p_0 in eq 18 also exhibits minimal variation with the changes in binding energy E_bind, provided that the incident electron energy is sufficiently high. Accordingly, the collision amplitude $(2\pi)^4 \times p_1p_2/p_0 \times f_\mathrm{ee}$ is virtually constant against both $\Delta\phi$ and E_bind values. This means that the incident electron energy is high enough if the observed target electronic structure information is independent of the energy. Thus the validity of the PWIA is experimentally verifiable, as will be demonstrated in Section **4.2**.

The high-energy conditions required for the PWIA can be relaxed by replacing the plane waves in the structure factor $\langle \boldsymbol{p}\Psi_\mathrm{f}|\Psi_\mathrm{i}\rangle$ ($=\langle \boldsymbol{p}_1\boldsymbol{p}_2\Psi_\mathrm{f}|\Psi_\mathrm{i}\boldsymbol{p}_0\rangle$) with distorted waves. Furthermore, the replacement is the simplest way to account for the presence of the ion in the collision, which is completely ignored in the PWIA. Hence it extends the impulse approximation to lower energies. This approximation is called the distorted wave impulse approximation (DWIA) and its TDCS is given[45,53] by
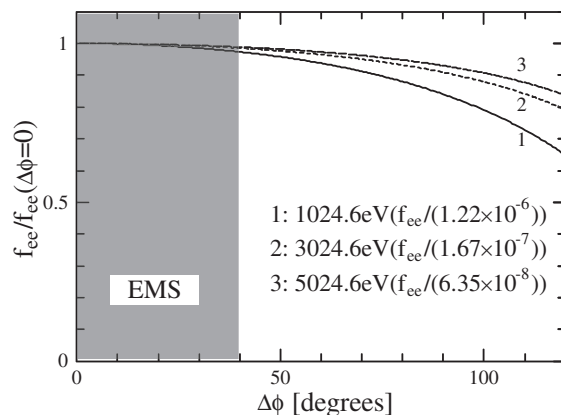
Figure 3. The $\Delta\phi$-angle dependence of f_ee in the symmetric noncoplanar geometry at $E_0 = 1024.6$, 3024.6, and 5024.6 eV for He 1s ionization. Each f_ee curve is normalized by division of its value at $\Delta\phi = 0°$. The normal $\Delta\phi$-angle range covered in the experiments is indicated by the shaded region.

$$\frac{\mathrm{d}^3\sigma_\mathrm{DWIA}}{\mathrm{d}\Omega_1\mathrm{d}\Omega_2\mathrm{d}E_1}$$
$$= (2\pi)^4\frac{p_1p_2}{p_0}f_\mathrm{ee}\sum_\mathrm{av}|\langle \chi^{(-)}(\boldsymbol{p}_1)\chi^{(-)}(\boldsymbol{p}_2)\Psi_\mathrm{f}|\Psi_\mathrm{i}\chi^{(+)}(\boldsymbol{p}_0)\rangle|^2 \qquad (21)$$

where $\chi^{(+)}(\boldsymbol{p}_0)$ is the distorted wave representing the incident electron generated in the static potential of the neutral target, and $\chi^{(-)}(\boldsymbol{p}_1)$ and $\chi^{(-)}(\boldsymbol{p}_2)$ are the distorted waves for the two outgoing electrons moving in the static potential of the residual ion.

It is also worthwhile to note that the structure factor $\langle \boldsymbol{p}\Psi_\mathrm{f}|\Psi_\mathrm{i}\rangle$ is an one-electron function, as it involves integration over the coordinates of the $(N-1)$-electrons of the ion for an N-electron target. Hence it is often described by

$$\langle \boldsymbol{p}\Psi_\mathrm{f}|\Psi_\mathrm{i}\rangle = (S_\alpha^f)^{1/2}\phi_\alpha(\boldsymbol{p}) \qquad (22)$$

where $\phi_\alpha(\boldsymbol{p})$ is the momentum space representation of the quasi-particle or Dyson orbital. The real number S_α^f is called the spectroscopic factor or pole strength, while the index α represents here the symmetry of the orbital. Then the TDCS of the PWIA is given by

$$\frac{\mathrm{d}^3\sigma_\mathrm{PWIA}}{\mathrm{d}\Omega_1\mathrm{d}\Omega_2\mathrm{d}E_1} = (2\pi)^4\frac{p_1p_2}{p_0}f_\mathrm{ee}\sum_\mathrm{av}S_\alpha^f|\phi_\alpha(\boldsymbol{p})|^2 \qquad (23)$$

Similarly, the TDCS of the DWIA is given by

$$\frac{\mathrm{d}^3\sigma_\mathrm{DWIA}}{\mathrm{d}\Omega_1\mathrm{d}\Omega_2\mathrm{d}E_1}$$
$$= (2\pi)^4\frac{p_1p_2}{p_0}f_\mathrm{ee}\sum_\mathrm{av}S_\alpha^f|\langle \chi^{(-)}(\boldsymbol{p}_1)\chi^{(-)}(\boldsymbol{p}_2)|\chi^{(+)}(\boldsymbol{p}_0)\phi_\alpha\rangle|^2 \qquad (24)$$

When a Hartree–Fock (HF) ground state is a good description of the initial target state Ψ_i, the HF-type ionized orbital may closely approximate the Dyson orbital. This is called the target HF approximation. In this case, S_α^f is identical to the probability of finding the one-hole configuration ϕ_α^{-1} in the configuration–interaction (CI) expansion of the final ion wave function Ψ_f and hence it satisfies the following sum rule.

M. Takahashi

Bull. Chem. Soc. Jpn. Vol. 82, No. 7 (2009) 755

$$\sum_{f} S_{\alpha}^{f} = 1 \qquad (25)$$

3. Experimental Techniques

Experimentally, the use of high incident electron energy (typically $E_0 \geq 1.2\,\mathrm{keV}$) imposes stiff requirements in order to obtain a workable signal count rate and a moderate energy resolution in parallel. For instance, the symmetric noncoplanar EMS cross section, which is inherently much smaller than the forward-scattering (e,2e) cross section, becomes smaller at higher incident electron energy. In addition, the overall energy resolution ΔE_{EMS}, which can be expressed by

$$\Delta E_{\mathrm{EMS}} = \sqrt{(\Delta E_0)^2 + (\Delta E_1)^2 + (\Delta E_2)^2} \qquad (26)$$

becomes lower at higher incident electron energy, because the energy resolution of an electron energy analyzer ΔE is usually inversely proportional to the electron pass energy E_{pass} ($\Delta E / E_{\mathrm{pass}}$ is constant).[57] These are the material reasons why developments of more sophisticated multichannel techniques have always been a core subject of EMS.

The modern multichannel techniques for EMS experiments, which have realized simultaneous detection of the two outgoing electrons in energy and momentum while achieving modest energy resolution by using the electron pre-retardation method,[57] were developed in 2002 by Takahashi et al.,[58] and later by Ren et al.[59] To illustrate the present stage of such multichannel techniques, the details and performance of the (e,2e) spectrometer developed by Takahashi et al.[58] are described in this section. The most advanced form of EMS, molecular frame EMS that enables one to look at molecular orbitals in three-dimensional form, will be discussed in Section **6**.

3.1 (e,2e) Spectrometer. Figure 4 shows the cross section of the (e,2e) spectrometer developed by Takahashi et al.[58] It is placed in a bell-shaped vacuum chamber (inner diameter = 998 mm), which is evacuated by a 3400 $\mathrm{dm^3\,s^{-1}}$ turbo molecular pump to the base pressure of about $3 \times 10^{-5}\,\mathrm{Pa}$. The ambient magnetic fields are reduced to lower than 2 mG by double μ-metal shields.

Major sections of the spectrometer are an electron gun, a sample inlet system equipped with eight gas-nozzles, a pair of decelerating electrostatic lenses in a conical shape, a spherical electron energy analyzer,[60] Herzog plates,[61] and a pair of position sensitive detectors (PSDs; RoentDek, DLD40). In short, incident electron beam (typical diameter = 1 mm) is produced by the electron gun that incorporates a tungsten filament with the Wehnelt electrode to control the crossover point, followed by a telefocus triple cylinder electrostatic lens. A current of typically several tens of μA is collected on a Faraday cup. Electron impact ionization occurs where the incident electron beam collides with gaseous targets from the eight gas-nozzles (inner diameter = 0.5 mm), which are directed towards the ionization point, forming a conical shape in order to have intense and uniform target gas densities. Scattered electrons are limited by a pair of apertures so as to pass only those with $\theta = 45°$ over the azimuthal angle ϕ_1 and ϕ_2 ranges from 70 to 110° and from 250 to 290° (i.e., the $\Delta\phi$-angle range from −40 to 40°). In the angular selection one of three pairs of
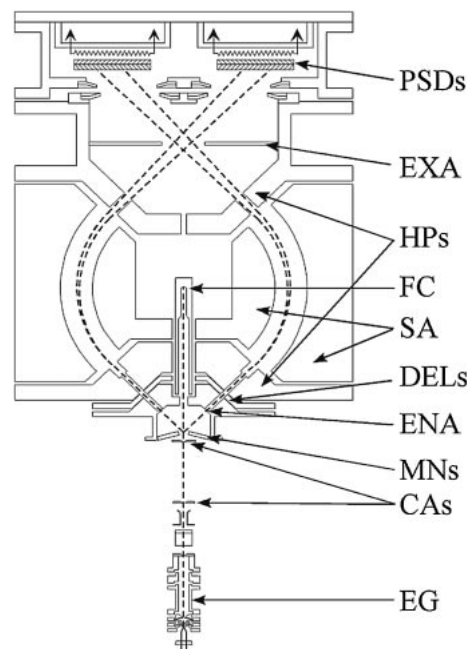
Figure 4. Cross section of an (e,2e) spectrometer, showing the electron gun (EG), collimating apertures (CAs), multi-gas-nozzles (MNs), entrance aperture (ENA), decelerating electrostatic lenses (DELs), spherical analyzer (SA), Faraday cup (FC), Herzog plates (HPs), exit aperture (EXA), and position sensitive detectors (PSDs). Adapted with permission from Ref. 58. Copyright 2002. American Institute of Physics.

apertures with $\Delta\theta = \pm 1.0$, 1.5, and 3.0° is used, in accordance with experimental requirements concerning energy resolution and/or collection efficiency. In the case when higher energy resolution is desired, the angle-selected electrons are pre-decelerated with the electrostatic lenses that were designed based on the triple rectangular lens system.[62] The spherical analyzer (mean radius = 100 mm) accepts the electrons passing through the apertures and lenses and then disperse them depending on their energies. The design of the analyzer is based on the study of Purcell,[60] and its parameters have been chosen symmetrically for ease of construction. The deflection angle is 90°, and the inner and outer radii are 85 and 115 mm, respectively. The fringing filed compensation is attempted by using the Herzog plates[61] at both the entrance and exit of the analyzer. The electrons are eventually detected with the PSDs placed behind the exit aperture. Since a spherical analyzer maintains azimuthal angles for the electrons, both energies and angles can be determined from their arrival positions at the detectors. Thus the joint use of the spherical analyzer and PSDs makes it possible to sample the (e,2e) cross section over a wide range of binding energy and ion recoil momentum simultaneously. This multichannel technique has not only significantly improved collection efficiency but also the accuracy of the experimental data compared with the conventional single channel measurements, as drifts in electron beam current and fluctuations in target gas density affect all channels in the same way.

3.2 Data Acquisition. Each PSD produces five separate output signals for each electron arrival: a time reference signal
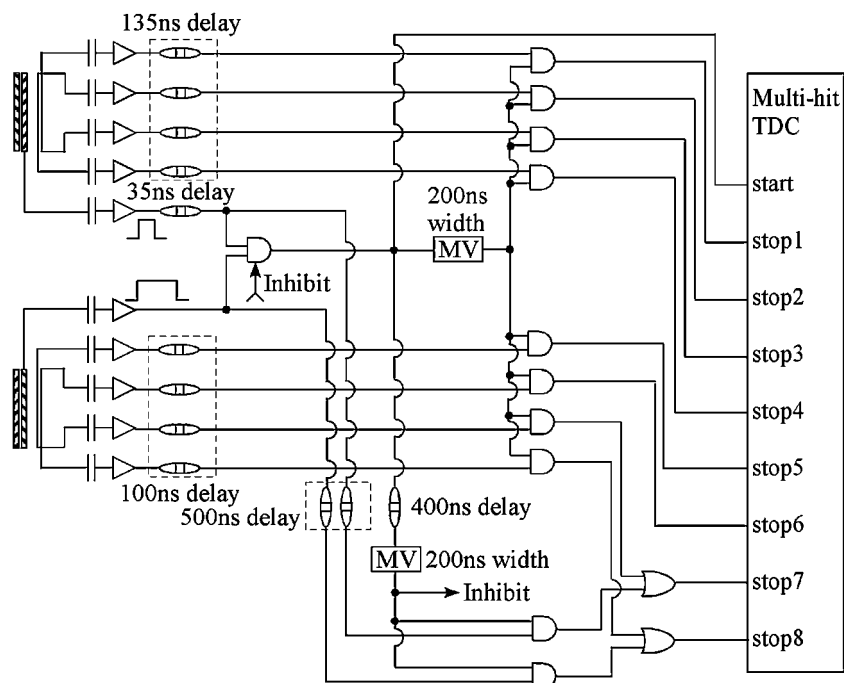
Figure 5. Schematic diagram of a signal processing electronics system for electron–electron coincidence experiments. On the diagram MV is a multivibrator and TDC is a time-to-digital converter.

from the micro channel plates (MCPs) stacked in the so-called Chevron configuration and two delayed signals from the ends of each of the two orthogonal delay lines for positional readout. Hence a coincidence event consists of ten signals. Such events are recorded in a computer after passing through a signal processing electronics system which is schematically shown in Figure 5.

The main features of the electronics system are:

(1) The two time reference signals from the PSDs are made to have 15 and 50 ns widths, whilst a delay time of 35 ns is given to the short (15 ns) pulse. AND output of the two time reference signals is used as a common start pulse of a time-to-digital converter (TDC; RoentDek, TDC8) with eight independent stop channels. The use of the AND function significantly reduces dead time of the TDC due mainly to accidental coincidence events in which two uncorrelated electrons produced in different events are detected accidentally, because the AND output is generated only when two electrons are detected within a short time interval.

(2) Delay times of 135 and 100 ns are given to the delay line signals associated with the short (15 ns) and long (50 ns) time reference pulses, respectively. These delay times are used to avoid any delay line signals overtaking the start pulse of the TDC. Arrival positions of the electrons at the PSDs are determined only by the time difference between the delay line signals, as the length of the delay line is fixed and the propagation speed of the electric signal on the line is constant. Thus the delay times of 135 and 100 ns do not affect the positional resolution of the PSDs.

(3) The AND function is applied to the delay line signals in order to extract only those associated with the AND output of the two time reference pulses. Then individual delay line signals are fed to the eight independent stop channels (1–8) of

the TDC, each of which has a time resolution of 0.5 ns and a capacity for up to 16 hits.

(4) Since one of the two time reference signals is always lost by the use of the AND function, the complete original time information is stored in a different way. After giving delay time of 500 ns to the short and long time reference pulses, the AND function is used to collect those associated with the 400 ns-delayed AND output of the time reference signals. Then the short and long pulses are merged with two of the delay line signals by the OR function, and the resulting OR outputs are measured at the stop channels (7 and 8) of the TDC.

In this way, this electronics system accumulates all the information needed for EMS studies, while giving the fastest possible time response. In addition, a delay line signal t_X and its counterpart t_{XX} from a PSD have the following relationship with the associated time reference signal t_{MCP}:

$$(t_X - t_{MCP}) + (t_{XX} - t_{MCP}) = \text{constant} \qquad (27)$$

Thus any electric noise signals can be easily separated from genuine electron signals by using the relationship of eq 27.

3.3 Energy and Angle Calibration.   Energy and angle calibration of the (e,2e) spectrometer can be made by using elastically scattered electrons that have the same energy to that of the incident electrons. Here a pair of masks is employed, which replaces the entrance apertures on the front of the decelerating lens stacks. Each mask has eleven small holes (0.5 mm in diameter) corresponding to azimuthal angles from 70 to 110° or from 250 to 290° in intervals of 4° at the $\theta = 45°$ direction. The space between the scattering point and the masks is field free, so there is no distortion of the electron trajectories. Thus a series of point like images of electrons with well-defined energies and angles can be observed. Figure 6 shows an example of such images, which were obtained for the
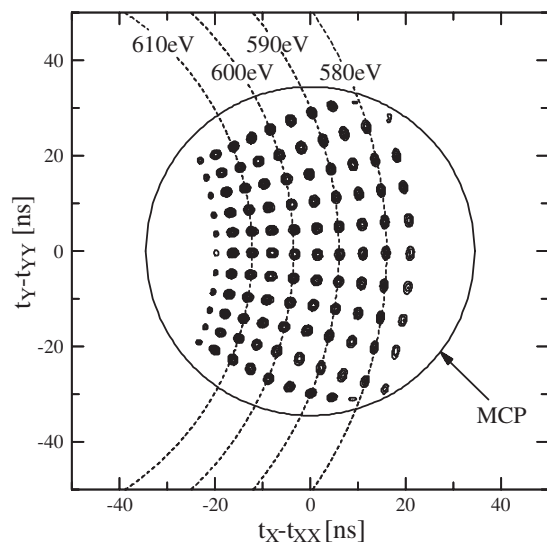
Figure 6.   Contour plot of an image of elastically scattered electrons, measured at a series of azimuthal angles as a function of incident electron energy. The broken lines are circles for 580, 590, 600, and 610 eV electrons. The solid circle represents the active area of the MCP. Adapted with permission from Ref. 58. Copyright 2002. American Institute of Physics.

Figure 7.   Typical time spectrum, which represents the number of coincidence events as a function of difference in arrival time between the two electrons detected.

azimuthal angle range from 70 to 110° by setting the analyzer pass energy to collect 600 eV electrons at the mean radius and by increasing the incident electron energy from 575 to 620 eV in 5 eV steps. It can be seen from the figure that at every incident-electron-energy value a concentric circle image consisting of eleven spots is measured and that the circles corresponding to different energies have their own radii. From these results a relationship between the arrival position and electron energy/angle can be obtained for each PSD, and it is used in the data analysis.

3.4 Data Analysis and Sample Results.   The experimental data set produced by the (e,2e) spectrometer is multidimensional; for each recorded event the raw data include information about the arrival positions of the two electrons detected and their arrival times. The positional information of the two electrons is converted to energies (E_1 and E_2) and azimuthal angles (ϕ_1 and ϕ_2), and their energy correlation is examined to collect EMS data associated with equal energy sharing ($E_1 = E_2$). Then the EMS data are stored in the individual binding energy (E_{bind}) and azimuthal angle difference ($\Delta\phi$) bins corresponding to small equal energy and angle intervals. Note that not all of the data are from true coincidence events, because at this stage the accidental coincidence events are not excluded. Hence, for each energy and angle bin selection of genuine EMS data are usually made by examining the time correlation between the two electrons detected.

Figure 7 shows a typical time spectrum, which was obtained by plotting the number of coincidence events as a function of difference in arrival time between the two electrons detected, i.e., $\Delta t_{\text{ee}} = t_{\text{MCP1}} - t_{\text{MCP2}}$. A true coincidence peak is clearly seen at around $\Delta t_{\text{ee}} = 0$ ns, which rides on constant background originating in the accidental coincidence events. The full width at half maximum (FWHM) of the peak is found to be about
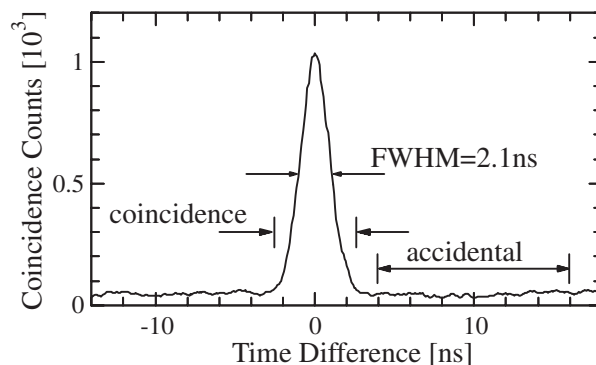
2.1 ns. It should be noted that the 2.1 ns value does not represent the intrinsic time resolution of the (e,2e) spectrometer, because the peak is constituted by contributions from various sets of two electrons having different energies and hence different times-of-flight. Thus the coincidence peak width becomes narrower when correction of the time-of-flight variation is made. The intrinsic time resolution of the present spectrometer is estimated to be 0.5–1 ns. The true coincidence counts N_{t} can be derived from the number of counts N_{c} in the coincidence window Δt_{c} and the number of counts N_{a} in the accidental window Δt_{a} by

$$N_{\text{t}} = N_{\text{c}} - \frac{N_{\text{a}}}{R} \tag{28}$$

where R is the ratio of the window widths ($R = \Delta t_{\text{a}}/\Delta t_{\text{c}}$). Its statistical uncertainty is given by

$$\Delta N_{\text{t}} = \sqrt{N_{\text{c}} + \frac{N_{\text{a}}}{R^2}} \tag{29}$$

Figure 8 shows an example of EMS data as a function of E_{bind} and $\Delta\phi$ in the form of a two-dimensional map, which were measured for Ar at $E_0 = 1.2$ keV. This map represents energy-momentum densities of the Ar valence electrons and contains a wealth of information about the target electronic structure such as binding energies, relative intensities, momentum distributions, and symmetries of the states involved. For example, the intensity distribution along the E_{bind} axis gives binding energy spectra at each $\Delta\phi$, as in the right panels (a) and (b) where the main band due to the Ar $3p^{-1}$ and $3s^{-1}$ primary ionization transitions as well as the satellite structure are seen. On the other hand, from the intensity distribution along the $\Delta\phi$ axis the momentum dependence of the (e,2e) cross sections or momentum profiles of individual transitions can be obtained, as in the bottom panels (c) and (d).

Presenting EMS data in the form of a two-dimensional map is one of the visible proofs of significant multichannel advantages. Effects of the multichannel technique may be measured by comparison in total acquisition time of data with the previous techniques. In order to obtain EMS data of this level in Figure 8, the single channel method used in early days requires more than several months and energy-dispersive or momentum-dispersive techniques developed in 1990's[33,39–44] makes it possible to obtain these data within several days.
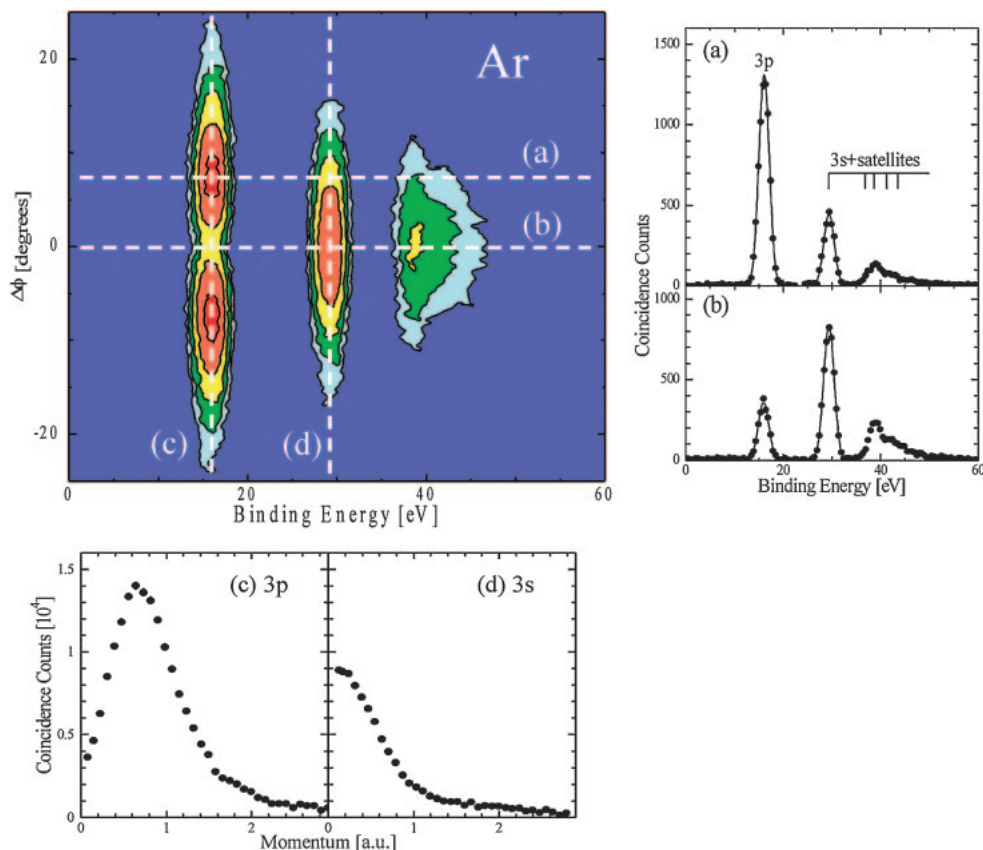
Figure 8. Two-dimensional plot of EMS data obtained for Ar at $E_0 = 1.2$ keV. The right panels (a) and (b) are binding energy spectra, which are generated by plotting the intensities of the two-dimensional data at $\Delta\phi = 0$ and $7°$ along the E_{bind} axis. The bottom panels (c) and (d) are momentum profiles for the 3p and 3s orbitals, which are generated by plotting the intensities at $E_{bind} = 15.8$ and 29.2 eV along the $\Delta\phi$ axis. Adapted with permission from Ref. 58. Copyright 2002. American Institute of Physics.

Presently this time has been shortened to only a few hours.[58] However, there is still ample room for improvement in collection efficiency, because a significant portion (ca. 99%) of the available EMS signal is wasted even with this latest multichannel technique. This fact does not imply a serious drawback for EMS but promises startling developments of the technique in future.

4. EMS Studies on One-Electron Processes

The thrust of recent EMS studies on one-electron processes, in which one of the target electrons is considered to have been removed from the corresponding HF orbital whilst other target electrons remain as they were, can be classified in two categories. The first focuses on the extraction of electronic structure information of various targets, while the second involves investigation of collision physics. Since insights gained in the first category can be established on the knowledge accumulated in the second one and vice versa, they are closely related to each other like "two sides of the same coin." In this section, we will see two showcase EMS studies on one-electron processes: rare gases by Miyake et al.,[63] and glyoxal and biacetyl by Takahashi et al.[64] Results of the two studies will be presented along with associated theoretical calculations and interpretations.

4.1 Rare Gases. Ionization processes of rare gases have long been a subject of fundamental importance as well as of in-

terest as a testing ground for many kinds of theoretical models. This is especially true for EMS. A large number of studies have been conducted so far at various incident electron energies for He,[45,53,65–74] Ne,[24,45,53,66,75,76] Ar,[28,45,53,55,58,63,65,66,77–80] Kr,[45,53,63,65,81] and Xe.[34,35,45,53,63,66,82–86] Through years of the outcome of the studies, it is generally believed that at small momenta below about 1.5 au both the PWIA and DWIA give a very good description of the binary (e,2e) reaction for the outer valence electron ionization with $E_0 >$ ca. 1 keV, although at larger momenta the DWIA is superior to the PWIA in reproducing the experimental results. This has been unquestionably confirmed by the study of Miyake et al.,[63] in which momentum profiles for the two outermost orbitals of rare gases have been obtained with high statistical precision over a wide range of momentum up to 3.6 au.

Figure 9 shows the $\Delta\phi$-angle integrated binding energy spectra of Ar, Kr, and Xe, obtained by Miyake et al.[63] at $E_0 = 2$ keV. Vertical bars represent ionization energies, indicating the np^{-1} and ns^{-1} primary ionization transitions and their satellites for Ar ($n = 3$), Kr ($n = 4$), and Xe ($n = 5$). It can be seen that although the instrumental energy resolution does not allow a complete separation of the spin–orbit components ($np_{3/2}^{-1}$ and $np_{1/2}^{-1}$ final ion states) of the np^{-1} primary ionization transition from each other, they are well separated from the associated ns^{-1} primary ionization transition. Hence, in the study of Miyake et al.,[63] np momentum profiles were
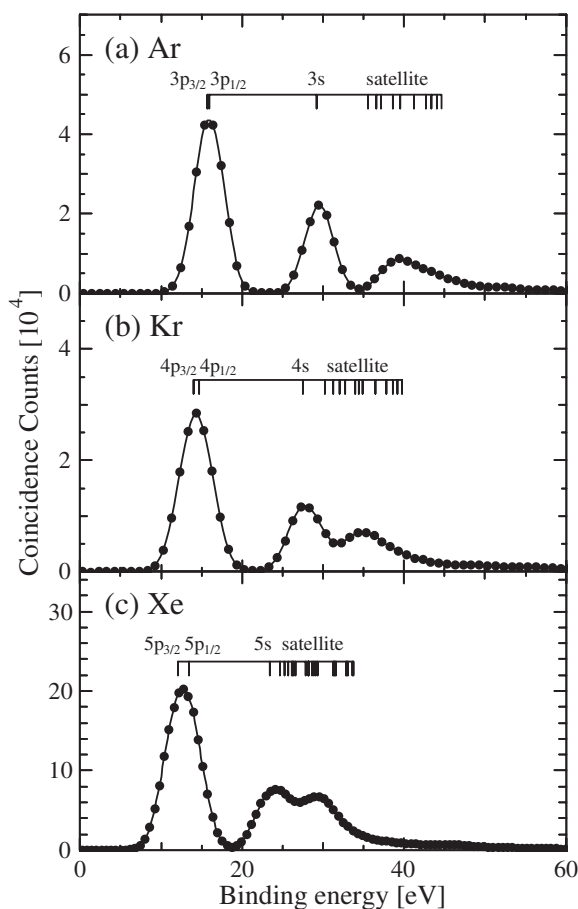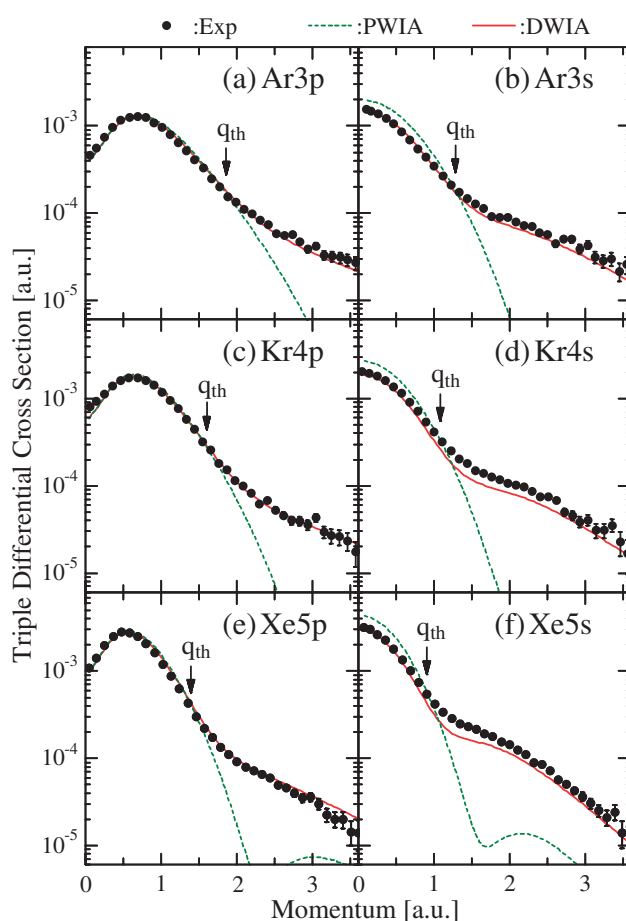
Figure 9. Binding energy spectra of (a) Ar, (b) Kr, and (c) Xe. Adapted from Ref. 63 with permission from the PCCP Owner Societies.

Figure 10. Comparison of momentum profiles between experiment and theory for the two outermost orbitals of Ar, Kr, and Xe. See text for details. Adapted from Ref. 63 with permission from the PCCP Owner Societies.

generated by plotting the number of true coincidence events originating from the corresponding np^{-1} primary ionization transition as a function of ion recoil momentum q, although they are the sum of contributions from the spin–orbit components ($np_{3/2}^{-1}$ and $np_{1/2}^{-1}$). On the other hand, ns momentum profiles were generated by plotting the number of true coincidence events associated with the binding energy ranges from 23 to 50 eV for Ar, from 21 to 48 eV for Kr, and from 19 to 45 eV for Xe. It means that the ns momentum profiles involve not only contributions of the ns^{-1} primary ionization transition but also those of its satellites that are attributed to ionization–excitation transitions in which one of the target electrons is ejected while some of the other electrons are excited. It should be noted that the momentum profile of a satellite is expected, within the target HF approximation, to have a shape similar to that of the corresponding primary ionization transition while its relative intensity is governed by the ratio of their spectroscopic factors. Thus the use of the wide binding energy ranges ensures that the spectroscopic factors of the ns momentum profiles for Ar, Kr, and Xe can be treated as unity.

Figure 10 shows the experimental momentum profiles obtained for the np and ns atomic orbitals of Ar ($n = 3$), Kr ($n = 4$), and Xe ($n = 5$). Also included in the figure are the associated theoretical momentum profiles calculated using the

DWIA and PWIA, which have been folded with the instrumental momentum resolution for direct comparison with the experiments. In this figure the momentum profiles are presented on a logarithmic scale in order to highlight the differences between them at large momenta where the (e,2e) intensities are relatively small. Although the experimental results are not absolute (e,2e) cross sections, one can compare those with theory by generating a common scale by taking advantage of the fact that the relative magnitudes of individual transitions are maintained in the experiments. The np experimental momentum profiles of Ar, Kr, and Xe are normalized to the DWIA momentum profiles by fitting areas of the experiments up to $q = 3.6$ au to those of theory. In the normalization procedure spectroscopic factors of 0.975, 0.977, and 0.976 predicted by the CI calculations of Dyall and Larkins[87] are assumed for Ar 3p, Kr 4p, and Xe 5p, respectively. Likewise, the PWIA momentum profiles are scaled by factors of 0.938 for Ar, 0.943 for Kr, and 0.954 for Xe, respectively, so that the area of each np momentum profile is the same as that of the corresponding DWIA one.

It is evident from Figure 10 that each experimental momentum profile exhibits its own characteristic shape; the np momentum profile has a maximum at around $q = 0.6$ au and its intensity falls off with the decrease in q, while the ns one has a

maximum at the momentum origin. Furthermore, we can see a tendency that both the np and ns momentum profiles become sharper as the target atom is heavier, as previously pointed out by Leung and Brion.[66] The shapes and tendency experimentally observed can be understood within the context of the PWIA, which directly connects the (e,2e) cross section with the electron momentum densities for individual ionization transitions or allows one to look at individual electron orbitals in momentum space (see eqs 18 and 23). Indeed the PWIA reproduces the experimental momentum profiles well, in terms of shape, at small momenta below q = ca. 1.5 au where most of the experimental intensity lies. Since the angular part of a wave function is invariant under the Dirac–Fourier transform, a certain electron orbital in position space has similar shape in momentum space. On the other hand, the radial part of a wave function is largely affected by the Dirac–Fourier transformation; high density at small r leads to high density at large q and vice versa. Thus the most diffuse orbital possesses the most sharply peaked momentum distribution. Spatial orbital patterns manifest themselves in momentum profiles in this way.

In spite of the good agreement between the shapes of the experiment and PWIA for $q < 1.5$ au, one does, however, notice some differences at large momenta. For ease of comparison momentum values q_{th}'s, at which the PWIA begins to deviate from the experiments, are indicated by arrows in Figure 10. Interestingly, q_{th} varies with the orbital and the target: q_{th} = ca. 1.8 and 1.3, 1.6 and 1.1, and 1.4 and 0.9 au for the np and ns momentum profiles of Ar, Kr, and Xe, respectively. These values follow the two trends. First, q_{th} for the outermost np orbital is always larger than that for the more tightly bound ns. Second, q_{th} shifts towards smaller momentum as the target is heavier. These two trends are associated with the (e,2e) reaction dynamics that the larger momentum region of the experiments involves contributions from the smaller r region, near to the nucleus, where potentials of the target atom and the residual ion may distort the incoming and outgoing electrons from plane waves. In fact, the DWIA results almost completely resolve the difference between experiment and PWIA over the entire momentum range covered.

Such superiority of the DWIA can be seen in terms of intensity also. The ns momentum profiles can check the intensities of the calculations, because the experiments are normalized for the np results. It can be seen from Figures 10b, 10d, and 10f that at small momenta the PWIA noticeably overestimates the experimental (e,2e) cross sections from the ns orbitals. To bring about agreement in intensity between PWIA and experiment for small momenta, the ns PWIA momentum profiles have to be multiplied by an additional factor of about 0.80. It implies, provided the PWIA prediction about intensity were valid, that the experimental ns momentum profiles have a spectroscopic factor value of 0.80, an unacceptable value that is too small against the expectation that the spectroscopic factor is unity. On the other hand, the DWIA meets the expectation that the spectroscopic factor value of every ns experimental momentum profile is unity, fully reproducing the experimental intensities. This observation indicates that the DWIA gives satisfactory descriptions of the ns and np momentum profiles of the noble gases in terms of not only shape but also of intensity, illustrating effects of electron wave distortion at the incident

electron energy employed. It also indicates that higher incident electron energy would be required to have satisfactory agreement between experiment and PWIA, concerning the intensity ratio of s- and p-type orbital ionization in particular.

4.2 Glyoxal and Biacetyl.   Investigation of functional groups, which give characteristic chemical properties to molecules, has been one of the most important subjects in chemistry. Molecules possessing two equivalent functional groups have particularly attracted interests of many researchers. For the understanding of intramolecular interactions between the identical functional groups, Hoffmann et al.[88,89] have proposed the concept of through-space (TS) and through-bond (TB) interactions. TS interaction originates from the direct overlap between the semi-localized orbitals of the two functional groups, and places their symmetric linear combination ($\phi+$) below the antisymmetric one ($\phi-$). In contrast, TB interaction, which occurs with participation of intervening bonds, may force the orbital ordering to be reversed. These TS and TB interactions are usually competitive and hence the orbital ordering depends on the molecule in question.

Glyoxal (CHOCHO) and its methyl-substituted congener, biacetyl, are among the first systems to be studied in terms of TS and TB interactions. In these systems symmetric and antisymmetric linear combinations of the two equivalent semi-localized orbitals (oxygen lone-pair orbitals) constitute the two outermost orbitals, the highest occupied molecular orbital (HOMO) and the next HOMO (NHOMO). Since reactivity and other properties of a molecule largely depend on the symmetry and electron density distribution of the HOMO, it is important to know which of the two interactions dominates. Although orbital energies of glyoxal and biacetyl have been precisely studied by photoelectron spectroscopy (PES), their assignments are mostly made with the aid of theoretical calculations. Thus one might desire to have unambiguous experimental evidence of the orbital orderings. EMS is best suited for this purpose.

Figure 11 shows the momentum profiles for the HOMO and NHOMO of glyoxal and biacetyl, measured by Takahashi et al.[64] at E_0 = 0.8, 1.2, and 1.6 keV. Here the momentum profiles at individual incident electron energies are placed on a common scale by integrating their intensities in the q^2-weighted form over a momentum range up to 1.9 au and by setting the integral value equal to unity, i.e., $\int |\phi_\alpha(q)|^2 q^2 dq = 1$. The large experimental uncertainties in the data at 0.8 keV are due mainly to a decrease in the quantum efficiency of the MCPs for electrons having lower energies.[90,91] Nevertheless, one may notice immediately from the figure that variation of the (e,2e) cross sections with incident electron energy is very marked below q = ca. 1 au for all the orbitals studied; the small-momentum components certainly reduce with the increase in incident electron energy. These observations are in a sharp contrast with the findings of previous studies on one-electron processes of simple targets such as rare gases,[19,28,65,77] H_2,[21] HF,[79,92,93] and CO,[94] in which the momentum profile shapes in the small momentum region were found to be independent of incident electron energy above values of a few hundred electronvolts. Unquestionably, the range of validity of the PWIA for glyoxal and biacetyl is substantially different from that for simple targets.

M. Takahashi

Bull. Chem. Soc. Jpn. Vol. 82, No. 7 (2009)   761
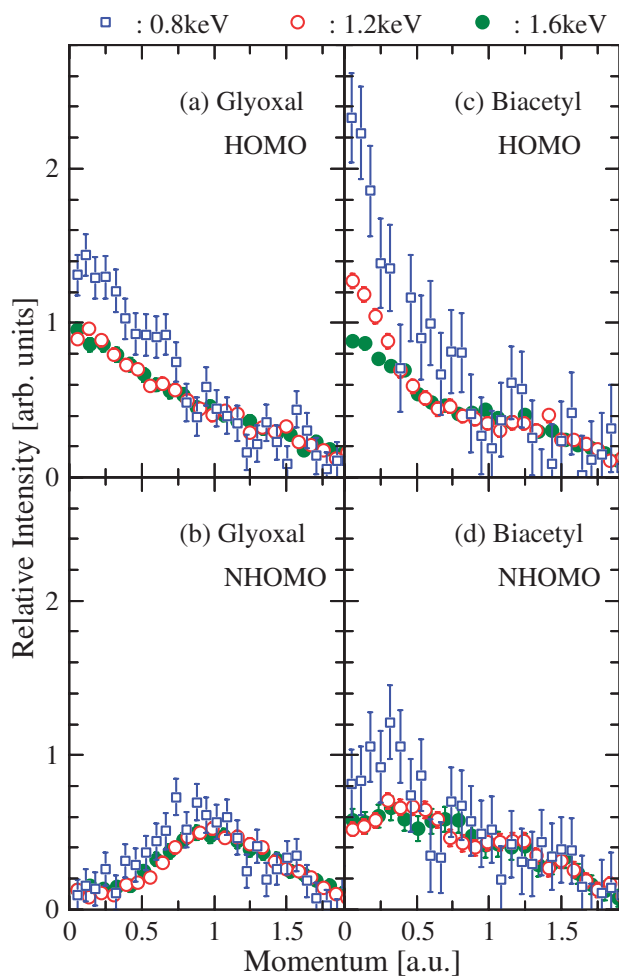
Figure 11. Incident electron energy dependence of momentum profiles for the two outermost orbitals of glyoxal and biacetyl. See text for details. Adapted with permission from Ref. 64. Copyright 2003. Institute of Physics.

It is also evident from Figure 11 that glyoxal and biacetyl exhibit different incident electron energy dependence compared to one another; the two molecules reach the high-energy limit at their own incident electron energies. In glyoxal, although the small-momentum components are reduced when the incident electron energy increases to 1.2 keV, the momentum profile shapes of the two orbitals are unaltered at a higher incident electron energy of 1.6 keV, indicating that the high-energy limit can be achieved at $E_0 = 1.2$ keV for the molecule. On the other hand, in biacetyl the small-momentum components fall off more and more as the incident electron energy increases up to 1.6 keV. Clearly, the incident electron energy needed to fulfil the PWIA conditions for biacetyl is higher than that for glyoxal.

Once the range of validity of the PWIA is known, one can discuss electron momentum distribution by using the momentum profiles measured under the corresponding experimental conditions. Let us bring our attention to the experimental data obtained for glyoxal at $E_0 = 1.2$ keV in Figure 11. It is evident that the momentum profiles of the two outermost orbitals are quite different from each other. The most significant difference lies in the intensity at the momentum origin; the HOMO

momentum profile shows a maximum at $q = 0$, while no appreciable intensity is observed for the NHOMO. Within the framework of the PWIA, the intensity of momentum profile at the momentum origin $\rho(q = 0)$ is given[30] by

$$\rho(q = 0) \propto \left| (2\pi)^{-3/2} \int \phi_\alpha(\boldsymbol{r}) \mathrm{d}\boldsymbol{r} \right|^2 \qquad (30)$$

where $\phi_\alpha(\boldsymbol{r})$ is the position space representation of the ionized orbital. This equation tells us that only totally symmetric orbitals can have nonzero intensity at the momentum origin. Hence the qualitative observation about the intensity near the momentum origin alone is enough to declare that the HOMO is totally symmetric $\phi+$ and accordingly the NHOMO can be attributed to the counterpart orbital $\phi-$. Thus the direct evidence for the dominant TB interaction is provided for glyoxal. Similar application of EMS to the TS and TB interactions has been made for biacetyl,[64] 1,4-diazabicyclo[2.2.2]octane,[30] 1,4-cyclohexadiene,[29] and norbornadiene.[29,95]

Another use of the experimental momentum profiles measured at the high-energy limit is to examine the quality of various theoretical wave functions. Figure 12 compares the experimental momentum profile for the glyoxal HOMO measured at $E_0 = 1.2$ keV with theoretical momentum profiles generated by the target HF approximation using several standard basis sets. Also included is theoretical momentum profile obtained by the density functional theory (DFT) with the target Kohn–Sham (KS) approximation[96–98] in which the Dyson orbital in eq 23 is replaced by the KS orbital.[99] In the figure the upper panel shows the calculated total energies. The right panels show position and momentum density contour maps of the orbital calculated by the DFT method using the AUG-cc-pVTZ basis set. While simple valence bond descriptions predict that the HOMO of glyoxal is a linear combination of the oxygen lone-pairs, it is clear from the position density map that the orbital is not composed of oxygen p atomic orbitals only. We can see considerable densities on the carbon atoms and participation of the carbon–carbon σ bond into the orbital, as expected from the experimental evidence of the dominant TB interaction. Furthermore, the orbital is slightly delocalized over the hydrogen atoms. Delocalization of the orbital is evident also in the momentum density map that shows "wrinkled" contours. It reflects the interference effects, often called bond oscillations,[68,100] due to multiple atomic centres participating in the bonding or anti-bonding interaction.

Bringing our attention back to the subject at hand, it can be seen from Figure 12 that all the theoretical momentum profiles reproduce the essential characteristics of the experiment, being that their maxima are at the momentum origin. However, different degrees of agreement between experiment and theory are observed, depending on the basis set employed. A HF calculation using the minimal basis set STO-3G (HF/STO-3G) fails to quantitatively reproduce the experiment. The 4-31G** basis set (HF/4-31G**) considerably lowers the total energy and reduces the discrepancy between the experiment and theory. Although inclusion of more primitive functions (HF/6-31G**) further lowers the total energy, the theoretical momentum profile remains almost unchanged. On the other hand, a surprising improvement in the momentum profile can be obtained by the inclusion of the diffuse functions (HF/
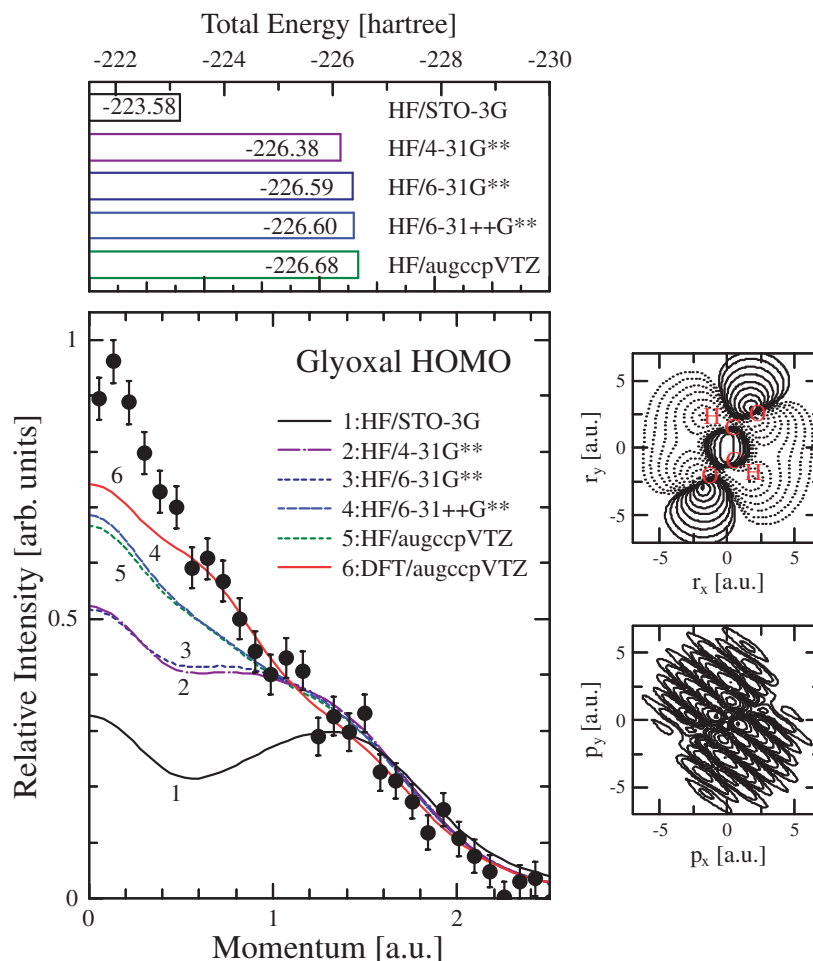
Figure 12. Comparison of theoretical momentum profiles of glyoxal HOMO with the experiments at $E_0 = 1.2$ keV. Upper panel represents the calculated total energies. Right panels show position and momentum density contour maps. Adapted with permission from Ref. 64. Copyright 2003. Institute of Physics.

6-31++G**), although the total energy change is minimal. Importance of the diffuse functions in describing small-momentum components, as pointed out by Bawagan and Brion,[101] reflects that EMS is very sensitive to small-momentum parts (diffuse parts in position space) of valence electrons, which play an important role in chemical reactions and molecular recognition. At the same time, we can see that a larger basis set, AUG-cc-pVTZ, (HF/augccpVTZ) does not bring about any noticeable improvement in the momentum profile. This means that the HF limit for the HOMO momentum profile is closely approached with the basis set of this level. Thus the discrepancies between experiment and theory at small momenta could not be resolved by more sophisticated HF wave functions. Instead, the discrepancies are substantially resolved by the DFT method (DFT/augccpVTZ), which involves functional terms to account for electron correlation. This observation accentuates the importance of electron correlation effects in quantitatively describing the HOMO density distribution of glyoxal. The remaining discrepancies between the experimental and DFT/augccpVTZ momentum profiles should be examined with more accurate Dyson orbitals, for example, those generated by calculating direct overlap of the initial and final CI wave functions.

The present study of Takahashi et al.[64] has revealed that the range of validity of the PWIA largely depends upon the target in question. To the best of my knowledge, this is the first example where a direct comparison of momentum profiles at different incident electron energies has been made for polyatomic molecules and the significant incident-electron-energy dependence of the small-momentum components has been observed. There is no doubt that such incident-electron-energy dependence originates in contributions of higher-order terms, which are not taken into account in the PWIA, to the (e,2e) cross section, and hence the observation would indicate that such higher-order effects may arise for polyatomics more commonly than have previously been supposed. Thus, the study of Takahashi et al.[64] has brought a new wave into the EMS of molecules, which would investigate more exhaustively the range of validity of the PWIA. For instance, similar incident-electron-energy dependence studies on one-electron processes have been conducted for O_2,[102] N_2O,[103] C_2H_4,[104,105] and C_2H_6[106] since then. These recent studies have shown that the range of validity of the PWIA may largely depend upon the electron orbital as well as the target, and that a more complete knowledge about higher-order effects or (e,2e) reaction dynamics is always vital, not only for its fundamental

importance but also in providing the physical basis to study energy-momentum densities of electrons in matter.

5. EMS Studies on Two-Electron Processes

The presence of satellite bands in binding energy spectra has been observed over a long period of time. It is now well documented that satellite bands provide a wealth of information about many-body electron correlation effects, thereby making it possible to investigate the electronic structures of atoms and molecules beyond the independent particle model. Direct evidence for such two-electron (or many-electron) processes, also known as shake-up, was originally given by PES.[107] Although the currently achievable energy resolution of EMS is rather poor compared with that of PES, EMS is able to provide more direct information about many-body structures. For instance, as noted in Section **4.1**, the Dyson orbital for a satellite is expected to be identical to that for its main band. Hence the manifold α to which the satellite belongs can be identified only by seeing the orbital-specific shape of the momentum profile. Furthermore, the relative magnitude of the satellite with respect to the main band is entirely governed by the ratio of the corresponding spectroscopic factors (S_α^f(satellite)/S_α^f(main)). Thus the spectroscopic factor value of a satellite can be determined experimentally on an absolute scale with the aid of the sum rule (see eq 25). Both of the momentum profiles and spectroscopic factors are fascinating materials, which are also offered by sophisticated quantum chemical theories such as the one-particle Green's function method along with the third-order algebraic diagrammatic construction scheme (ADC(3))[108–111] and the symmetry adapted cluster CI (SAC-CI) method.[112–116] EMS can, therefore, serve as an ideal bridge to connect quantum chemical calculations with the actual electronic structures.

Indeed, a large number of EMS studies along the above line were performed for various kinds of targets,[45–54] and the stream of studies of this kind has been flowing steadily up until now. During the last decade over thirty publications[27,72,86,103,117–147] have been successfully produced, involving studies on noble gases,[72,86] hydrocarbons,[123–129] halogen-substituted hydrocarbons,[130–135] five-membered aromatic heterocyclic molecules,[27,136–138] cage compounds,[139–145] and large molecules of biological interest.[146,147]

In this section, we will see two new streams of EMS studies on two-electron processes. One is motivated by interest in most directly probing the correlated motion of electrons, in two-electron systems, He[72,74] and H$_2$.[148] Another is a comparative study of binding energy spectra by means of PES and EMS,[86] which aims to achieve a more generalized understanding of ionization processes.

5.1 Two-Electron Systems: He and H$_2$. The study of electronic transitions in two-electron systems, He and H$_2$, is a fundamentally important issue, because the targets present two of the simplest cases for the investigation of electron correlation effects in a few-body Coulomb system. Of special interest are simultaneous ionization–excitation processes of the targets, in which one of the two target electrons is ejected while another is raised to an empty orbital. Since electron correlation is absent in the one-electron final ion state, EMS experiments on the ionization–excitation processes can directly probe
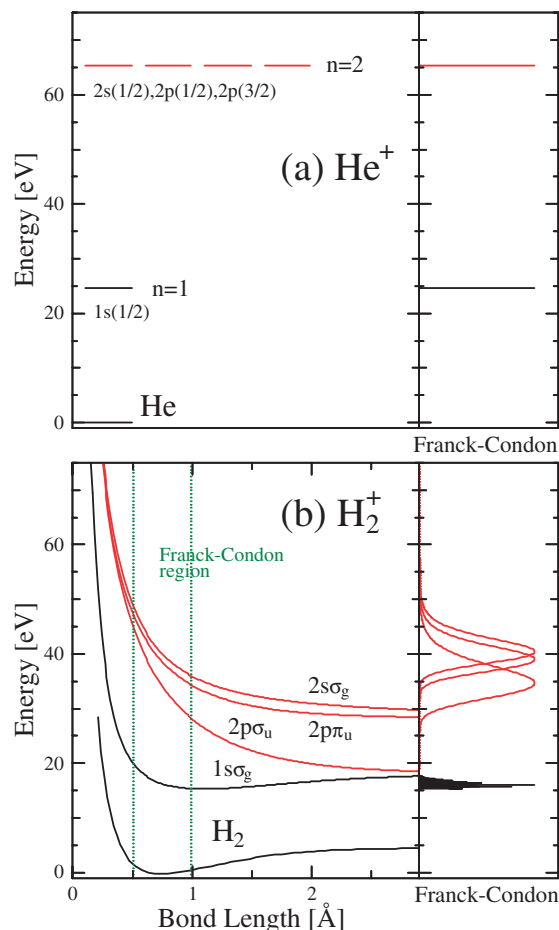
Figure 13. Energy diagrams of ionic states and calculated Franck–Condon patterns of individual transitions from their neutral ground states to the ionic states for (a) He and (b) H$_2$.

electron correlation in the initial neutral target state. Despite the importance, however, most of previous EMS experiments on He and H$_2$ were limited to the primary ionization processes that leave the residual He$^+$ and H$_2^+$ ions in their ground states. Furthermore, the pioneering studies on the ionization–excitation processes of He[68,69,71] and H$_2$[71,149,150] have been hampered from arriving at firm conclusions mainly by their extremely small cross sections, which are about two orders of magnitude smaller than the cross sections for the primary ionization processes. Thus application of the latest multi-channel technique[58] is crucial.

The EMS experiments on the two isoelectronic systems He[72,74] and H$_2$[148] are complementary to each other for the following three reasons. First, theoretical calculations of the (e,2e) cross section beyond the PWIA are technically feasible for He, but as yet they are very difficult for H$_2$ owing to its two-centre nature in the electron scattering potential. Second, as illustrated in Figure 13, the $n = 2$ state of He$^+$ is constituted by the 2s ^{2}S(1/2), 2p ^{2}P(1/2), and 2p ^{2}P(3/2) degenerate sublevels, while in H$_2^+$ the corresponding 2sσ_g, 2pσ_u, and 2pπ_u sublevels are energetically separated from each other and hence they can be resolved experimentally. Third, the $n = 2$ transition of He is separated in binding energy from
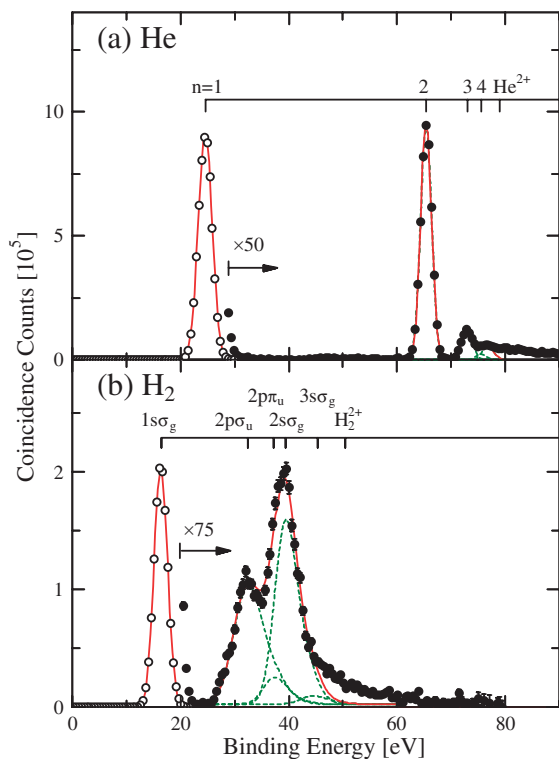
Figure 14. Binding energy spectra of He and H_2, obtained at $E_0 = 1.2$ keV. Note that the spectra responsible for two-electron processes are scaled by a factor of 50 for He and 75 for H_2. Adapted with permission from Refs. 74 and 148. Copyright (2007) and copyright (2003) by the American Physical Society.

the adjacent $n = 3$ transition, so it is relatively easy to have momentum profile at high precision. On the other hand, for H_2 the bands for the $2s\sigma_g$, $2p\sigma_u$, and $2p\pi_u$, as well as other ionization–excitation transitions are intrinsically broad in binding energy spectra due to the dissociative nature of the ion excited states and hence the bands significantly overlap with each other. Thus a deconvolution procedure with curve fitting is required to obtain momentum profiles for the $2s\sigma_g$, $2p\sigma_u$, and $2p\pi_u$ transitions separately, for which relatively better statistics of experimental data are desired.

Figure 14 shows $\Delta\phi$-angle integrated binding energy spectra of He reported by Watanabe et al.[74] and of H_2 by Takahashi et al.,[148] both of which have been measured at $E_0 = 1.2$ keV. Upright bars indicate vertical ionization energies, showing transitions of He (H_2) to the $n = 1$ ($1s\sigma_g$) ion ground state and the $n = 2$ ($2s\sigma_g$, $2p\sigma_u$, and $2p\pi_u$) ion excited states as well as the double ionization threshold. Note that the portion of each spectrum responsible for two-electron processes is scaled by a factor of 50 for He and that of 75 for H_2 for ease of comparison. Also included in the figure are fitting curves to separate the contributions of individual transitions from those of adjacent ones. The fitting curves are represented by the broken lines and their sum by the solid lines. In the fitting procedure, for He a Gaussian curve with a width of the instrumental energy resolution ($\Delta E_{EMS} =$ ca. 2.4 eV FWHM at $E_0 = 1.2$ keV) was attributed to each band. On the other hand, for H_2 Frank–Condon overlaps of the initial and final states were calculated
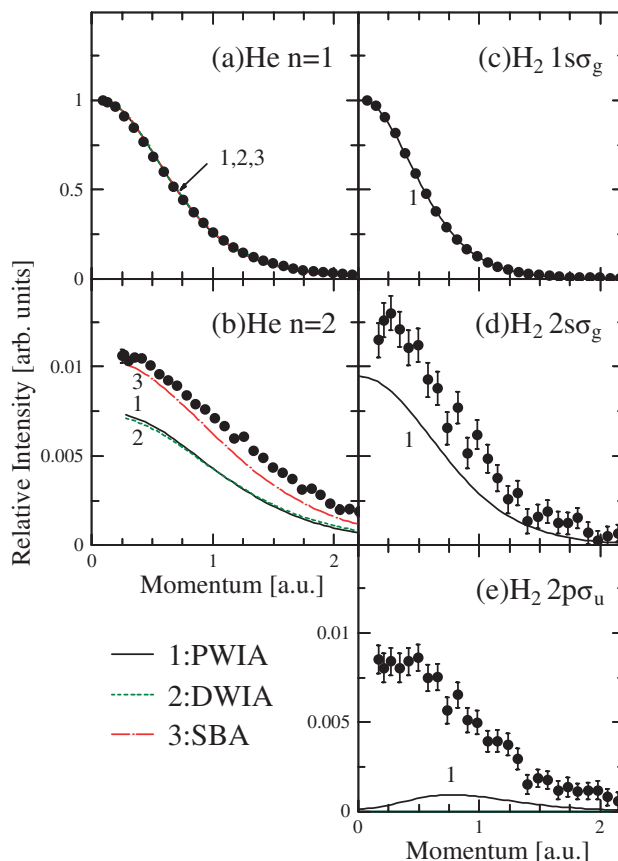
Figure 15. Comparison of momentum profiles at $E_0 = 1.2$ keV between experiment and theory for the (a) $n = 1$ and (b) $n = 2$ transitions of He and for the (c) $1s\sigma_g$, (d) $2s\sigma_g$, and (e) $2p\sigma_u$ transitions of H_2. Adapted with permission from Refs. 74 and 148. Copyright (2007) and copyright (2003) by the American Physical Society.

for the relevant transitions by using the potential energy curves of Sharp[151] and the BCONT program of Le Roy.[152] The results were folded with the instrumental energy resolution and were subsequently employed for the curve fitting. A similar fitting procedure was repeated for a series of binding energy spectra at each $\Delta\phi$ in order to produce momentum profiles.

Figure 15 shows the experimental momentum profiles for the $n = 1$ and 2 transitions of He and the $1s\sigma_g$, $2s\sigma_g$, and $2p\sigma_u$ transitions of H_2 thus obtained. Also included in the figure are associated theoretical momentum profiles generated by using the PWIA with CI wave functions that reproduce 98.6% of the correlation energy for He[72,74] and 99.5% for H_2[150] respectively. Note that He has additional theoretical results: DWIA momentum profiles and second-order Born approximation (SBA) momentum profiles.[74] The former is helpful to see how the electron wave distortion affects the momentum profiles, while the latter takes the contributions from the two-step (TS) mechanisms[153,154] into account, as will be discussed later. For comparison between experiment and theory, all the $n = 1$ momentum profiles of He ($1s\sigma_g$ of H_2) were height-normalized independently so that the values of their maxima, the intensities at $\Delta\phi = 0°$, become equal to unity. The normalization factors obtained for the $n = 1$ results of He ($1s\sigma_g$ of H_2) were subsequently applied to the $n = 2$ ($2s\sigma_g$ and

M. Takahashi

Bull. Chem. Soc. Jpn. Vol. 82, No. 7 (2009)   765

2pσ$_u$) momentum profiles. The present normalization procedure is justified by the findings of the previous studies on He[45,53,65–74] (H$_2$[21,67,71,149,150]) that the PWIA provides a very good description of the $n = 1$ (1sσ$_g$) transition at incident electron energy above values of a few hundred electronvolts. Indeed we can see in Figure 15 the satisfactory agreement between the $n = 1$ (1sσ$_g$) experimental and PWIA momentum profiles.

The issue to be discussed here is that the experimental momentum profiles for the ionization–excitation processes are substantially different from those obtained by the PWIA calculations. Let us consider the H$_2$ results first. The most striking feature of the H$_2$ results may be the difference in symmetry between the 2pσ$_u$ experimental and PWIA momentum profiles. Basically, the PWIA requests the 2pσ$_u$ momentum profile to exhibit p-type (ungerade) symmetry with zero intensity at the momentum origin, as is evident from eq 18, and indeed the 2pσ$_u$ PWIA momentum profile is in accordance with this symmetry consideration. However, the experimental result clearly exhibits s-type (gerade) symmetry with its maximum at the momentum origin. Thus we come to see unexpected difference in symmetry between experiment and PWIA in the 2pσ$_u$ channel, while in the 2sσ$_g$ channel the experiment shows s-type (gerade) symmetry and it is in good accord with the PWIA prediction. Furthermore, the difference in intensity between experiment and PWIA is also noticed and it is much larger in the 2pσ$_u$ channel than in the 2sσ$_g$ channel.

Understanding of the above observations is totally beyond the reach of PWIA, because the symmetry difference in the 2pσ$_u$ channel cannot be resolved even by using the exact target wave function. Hence, a possible clue for understanding the observations may be to consider higher-order effects that the first-order PWIA does not take into account. For this purpose, the plane wave Born series model is particularly attractive, as each higher-order term can be attributed to a particular mechanism of the (e,2e) collision. According to this model, Tweed[154] has shown that the second-order Born series can be split into five terms; the first (T_2^{ai}) is related to channel coupling, the next two (T_2^{ie} and T_2^{fe}) have their equivalents in the first-order distorted wave model, and the last two (T_2^{td} and T_2^{pd}) correspond to the TS mechanisms.[153] Amongst these five terms lie the key attributes responsible for the present observations.

One can rule out first a possibility that the observations originate in the first term (T_2^{ai}) of Tweed,[154] as effects of interchannel coupling in the ionization continuum have been proven to be negligibly small in EMS.[80] This is in a sharp contrast to high-energy photoionization where target states with different angular momentum, which are close in energy, are mixed through interchannel coupling in the continuum.[155]

The next two terms (T_2^{ie} and T_2^{fe}) of Tweed[154] describe elastic scattering of the incident electron followed or preceded by the (e,2e) collision of the incident electron with a certain target electron. Clearly, these terms allow ionization–excitation processes to occur only through the shake-up mechanism, in which, for example, the incident electron interacts with and knocks out one of the two target electrons and then another target electron is excited as a result of relaxation of the residual ion due to a sudden change in potential. In this regard, the role

of the two terms (T_2^{ie} and T_2^{fe}) for the ionization–excitation processes is to probe, in the second-order interaction between the projectile and target, momentum profiles of the 2sσ$_g$ and 2pσ$_u$ excited molecular orbital components of the initial target wave function. Hence, the momentum profiles may be different from the PWIA predictions, as some distorted wave effects are possible in the elastic scattering processes involved. An insight into such distorted wave effects can be gained, though indirectly, from the $n = 2$ DWIA momentum profiles for the isoelectronic system, He. It is evident from Figure 15b that the DWIA momentum profile is almost indistinguishable from the PWIA one as long as they are plotted on a linear scale. The minute difference between DWIA and PWIA can be seen mainly at large momenta only when they are presented on a logarithmic scale like Figure 10. We can, therefore, conclude that the distorted wave effects or the two terms (T_2^{ie} and T_2^{fe}) are not a principal source of the observations, in particular for the symmetry difference in the 2pσ$_u$ channel.

The last two terms (T_2^{td} and T_2^{pd}) of Tweed[154] thus remain, and indeed they can give a rational explanation for the H$_2$ results. The T_2^{td} and T_2^{pd} terms represent the two-step 1 (TS1) and two-step 2 (TS2) mechanisms,[153] respectively. The simplest scenario of the TS1 mechanism is that one of the two 1sσ$_g$ target electrons is ejected due to interaction with the incident electron and it raises the other 1sσ$_g$ electron to an excited orbital on its way out of the target. On the other hand, the TS2 mechanism allows the incident electron to interact with the target twice, and its simplest scenario is that one of the two target electrons is ejected and another electron is raised due to successive collisions of the incident electron with the target. Here, let us take the TS2 as a representative of the TS mechanisms in the following discussion, because the same arguments can be applied in the TS1 case.

If we adopt a very simple H$_2$ wave function $\Psi_i = \phi_0(\mathbf{r}_1)\phi_0(\mathbf{r}_2)$, the TS2 mechanism or the T_2^{pd} term can be described, according to the formalism of Tweed,[154] in the following form:

$$T_2^{pd} = 2^{-1} \int d\mathbf{p}' (p_0{}^2 + 2\varepsilon_0 - 2\varepsilon_{0,\mu} - p'^2 + i\varepsilon)^{-1}$$
$$\times (\pi K_a)^{-2} \langle \phi_{\mu'} | \exp(i\mathbf{K}_a \cdot \mathbf{r}_2) | \phi_0 \rangle$$
$$\cdot (\pi K_b)^{-2} \langle \phi_\mu | \exp(i\mathbf{K}_b \cdot \mathbf{r}_1) | \phi_0 \rangle \qquad (31)$$

where $\mathbf{K}_b = \mathbf{p}_0 - \mathbf{p}'$, $\mathbf{K}_a = \mathbf{p}' - \mathbf{p}_a$, and ε_0 and $\varepsilon_{0,\mu}$ represent energies of the initial and intermediate target states respectively. It should be noted that each of the two matrix elements in eq 31 is similar to that of the first-order plane wave Born model (see eq 2), and that the essential structure of this equation is not altered when a more sophisticated wave function is used. For the sake of further simplicity, let us suppose, for instance, that μ is a continuum state and that μ' is an excited state of the residual ion H$_2^+$. Then we clearly see that the ionization–excitation processes can occur by two sequential collisions of the electron projectile with different target electrons, namely the (e,2e) primary ionization process to the 1sσ$_g$ ground ion state of H$_2^+$, followed by a single excitation process to an excited ion state from the 1sσ$_g$ state. The excitation process involved must be dominated by forward scattering or pseudo-photon-impact (see eq 1 with an attention to the fact that the cross section is inversely proportional to the square of the

momentum transfer value), under the present experimental conditions where energies of both the incoming and outgoing electrons are very high compared with the energy loss. Hence the symmetry property of contributions from the TS mechanisms to the (e,2e) cross section is essentially determined by the preceding primary ionization process and would show little dependence upon the final ion state produced. Thus symmetry properties of contributions from the TS terms to the $2s\sigma_g$ and $2p\sigma_u$ momentum profiles must be identical to each other as well as to that of the $1s\sigma_g$ PWIA momentum profile.

However, a difference between the contributions from the TS terms to the $2s\sigma_g$ and $2p\sigma_u$ momentum profiles may appear in intensity, because the excitation process to the $2s\sigma_g$ state from the $1s\sigma_g$ state is a non-dipole transition whereas that to the $2p\sigma_u$ state is a dipole one. By considering again that the excitation process is dominated by forward scattering or pseudo-photon-impact, the magnitude of the TS contributions should be much larger for the "optically allowed" $2p\sigma_u$ transition than for the "optically forbidden" $2s\sigma_g$ transition. As a result, we can reach the following conclusion. The $2p\sigma_u$ experimental intensity can be significantly enhanced by the TS mechanisms and the symmetry difference would arise with respect to the PWIA prediction. On the other hand, for the $2s\sigma_g$ channel contributions from the TS mechanisms are very small compared to those of the PWIA mechanism and the symmetry of the momentum profile is maintained. In this way, Takahashi et al.[148] have arrived at and proposed in 2003 the rational explanation for the H_2 results.

Since then, Takahashi and his co-workers have begun to pile up the facts. The first fact can be seen by getting back to the $n = 2$ experimental momentum profile of He in Figure 15b. It is clear that the experiment exhibits noticeably larger intensity than the PWIA prediction, although they are in a good agreement in terms of symmetry. These observations are entirely consistent with the explanation for the H_2 results and one may conceive in the natural way what happens as the following; the $n = 2$ experiment is composed of contributions from the transitions to the 2s $^2S(1/2)$, 2p $^2P(1/2)$, and 2p $^2P(3/2)$ degenerate sublevels, and each contribution is further divided into contributions from the TS mechanisms with gerade symmetry and those from the PWIA mechanism. The next fact comes from developments of a SBA method by Watanabe et al.,[74] which have made it possible to evaluate the (e,2e) cross sections while incorporating the TS mechanisms. The result is fully as expected; the $n = 2$ SBA momentum profile reproduces satisfactorily the experiment, as can be seen from Figure 15b. Thus the explanation proposed by Takahashi et al.[148] is to a considerable extent acceptable even at the present stage. The last fact that Takahashi and others have deduced is the most direct one, in which EMS experiments on the ionization–excitation processes of H_2 have been carried out by Asano et al.,[156] at three different incident electron energy values ($E_0 = 1.2$, 2.0, and 4.0 keV) with higher precision having been achieved. The results have been successfully compared with associated SBA calculations by Watanabe and Takahashi,[157] although they are not depicted here (they will be reported in the following papers[156,157]). Briefly, the experimental and theoretical EMS studies[156,157] have unambiguously confirmed that the relative intensities of the $2s\sigma_g$ and $2p\sigma_u$

transitions with respect to the $1s\sigma_g$ transition as well as that of the $2p\pi_u$ transition certainly vary with the incident electron energy. The studies have also revealed that the $2s\sigma_g$, $2p\sigma_u$, and $2p\pi_u$ transitions approach in their own ways the high-energy limit where the PWIA is valid. Furthermore, the studies have shown that interference between the terms, which constitute second-order (e,2e) scattering amplitude as $f_{(e,2e)} = f_{PWIA} + f_{TS1} + f_{TS2}$, is the key to quantitatively understand the (e,2e) reaction dynamics at the low or intermediate incident electron energy values examined. Nevertheless, further efforts are required to completely settle the issue concerning the roles of higher-order terms, especially for stereodynamics of electron-H_2 collisions that will be discussed in Section **6**. In this respect, I would note again here that investigation of electronic structure and that of (e,2e) collision physics are closely related to each other like "two sides of the same coin."

5.2 Xe.   Ionization of the Xe atom is a process of particular interest for studying atomic many-electron processes. In fact, a large number of experimental studies have been conducted for this 54-electron system using various methods such as photon-, electron-, and positron-impact ionization cross section measurements,[158–160] PES,[161,162] and EMS.[35,53,82,83] Hence one may want to make comparisons of data by different methods for investigating what can be the common concept in the ionization mechanism, independent of the projectile species. The binding energy spectra by PES and EMS are especially attractive for this purpose, as they are generally believed to be equivalent, provided the projectile energy is sufficiently high; when the ionized electron emerges from the target potential quickly enough, the ionization intensity does not depend on the projectile species and it can be described mainly by many-electron correlation in the final state of the ion produced. According to this approximation, the relative intensities in the binding energy spectrum are equal to the spectroscopic factors of the corresponding final ion states, which determine the probability of finding the ion in the pure one-hole state. Thus one may be able to directly compare the binding energy spectrum by EMS with that by high-energy PES (HEPES) in terms of the spectroscopic factor.

Indeed such an attempt was made for Xe, by Braidwood et al.[82] They measured an EMS binding energy spectrum at high energy-resolution of 1.06 eV FWHM and at $E_0 = 1.0$ keV. The results were successfully compared with spectroscopic factors derived from a HEPES spectrum by Svensson et al.[162] using Al Kα X-ray, except for some satellite bands for which relative band intensities in the HEPES spectrum are found to be influenced by the atomic ground-state correlations that change most significantly the intensity of the $5s^{-1}$ main band and the continuous spectrum.[163] Furthermore, although the HEPES spectrum covers the binding energy range up to 220 eV involving ionization transitions of the valence 5p, 5s, and inner shell 4d, 4p, 4s electrons, the study of Braidwood et al.[82] was limited to ionization of the valence electrons. Due to the absence of EMS data above 44 eV, Brunger et al.[83] reported an EMS spectrum for the 4d electron ionization, but it covers only the specific energy region of 62–74 eV. Clearly, attempts at comparison over a wide binding energy range including as many bands as possible would be desired, because they make the most stringent assessment.

M. Takahashi

Bull. Chem. Soc. Jpn. Vol. 82, No. 7 (2009)   767
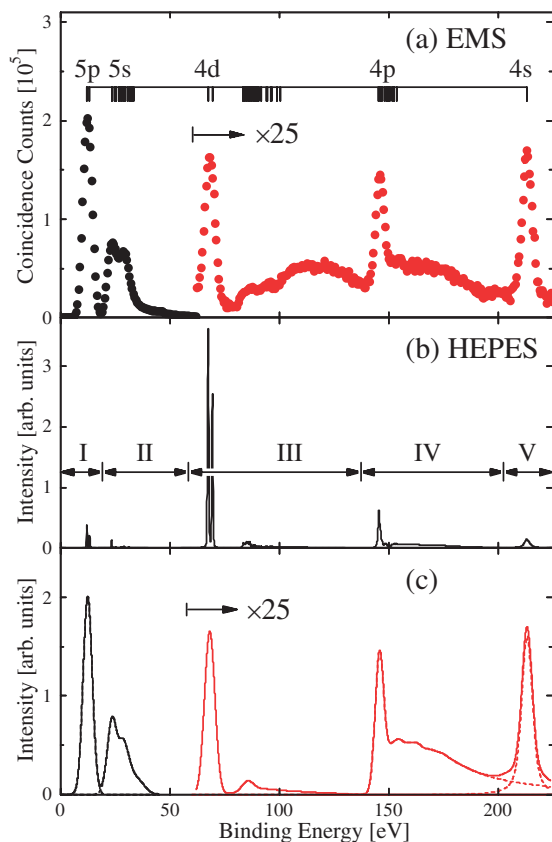
Figure 16. (a) EMS spectrum of Xe obtained at $E_0 = 2.1\,keV$. Note that the spectrum above 62 eV is scaled by a factor of 25. (b) HEPES spectrum of Xe measured by Svensson et al. [Ref. 162] using Al Kα X-ray. (c) Results of a least-squares fit to the EMS spectrum. See text for details. Adapted with permission from Ref. 86. Copyright (2007) by the American Physical Society.

Under these circumstances, Takahashi et al.[86] have carried out an EMS experiment on Xe at $E_0 = 2.1\,keV$ while covering a wide binding energy range of 0–220 eV. The measured $\Delta\phi$-angle integrated EMS spectrum of Xe is presented in Figure 16a. Note that the spectrum above 62 eV is scaled by a factor of 25 to make it easier to see bands due to the inner shell electron ionization. On the other hand, Figure 16b shows the HEPES spectrum of Svensson et al.,[162] which was digitized from the literature.

For EMS and HEPES studies on Xe the DWIA and the sudden approximation[164,165] have been widely used. Within these approximations, the relative intensities by PES and EMS, I_{PES} and I_{EMS}, can be written as

$$I_{PES} \propto S_\alpha^f \times |\langle \phi_{\varepsilon\alpha}|\boldsymbol{r}|\phi_\alpha\rangle|^2 \tag{32}$$

$$I_{EMS} \propto S_\alpha^f \times |\langle \chi^{(-)}(\boldsymbol{p}_1)\chi^{(-)}(\boldsymbol{p}_2)|\chi^{(+)}(\boldsymbol{p}_0)\phi_\alpha\rangle|^2 \tag{33}$$

Here $\phi_{\varepsilon\alpha}$ is a continuum wave for describing the photoelectron. Let us recall here that the Dyson orbital ϕ_α for a satellite band is the same as that for its main band when electron correlation in the initial target state is neglected. Hence, the spectroscopic factor S_α^f governs the relative intensity of a satellite with respect to its main band in both the EMS and HEPES spectra. Note that this aspect is valid as long as one adopts a first-order

approximation, such as the DWIA and PWIA, which assumes the electron projectile interacts with the target only once. For making a comparison between EMS and HEPES data into practice, however, one must take into consideration the difference in the orbital characteristic nature between the momentum profile $|\langle \chi^{(-)}(\boldsymbol{p}_1)\chi^{(-)}(\boldsymbol{p}_2)|\chi^{(+)}(\boldsymbol{p}_0)\phi_\alpha\rangle|^2$ and the square of the dipole matrix element $|\langle \phi_{\varepsilon\alpha}|\boldsymbol{r}|\phi_\alpha\rangle|^2$.

In the study of Takahashi et al.,[86] a comparison of the EMS and HEPES spectra was made as follows. First, the HEPES spectrum was cut into five pieces, as indicated by I–V in Figure 16b, so that each piece includes one of the $5p^{-1}$–$4s^{-1}$ main bands and a cluster of satellites at its higher energy. Second, the five pieces were individually folded with the EMS instrumental energy resolution and the resulting model spectra were subsequently employed as fitting curves to reproduce the EMS spectrum by summing them with appropriate weight factors. The fit to the EMS spectrum is shown in Figure 16c where the broken lines represent the fitting curves and the solid line their sum.
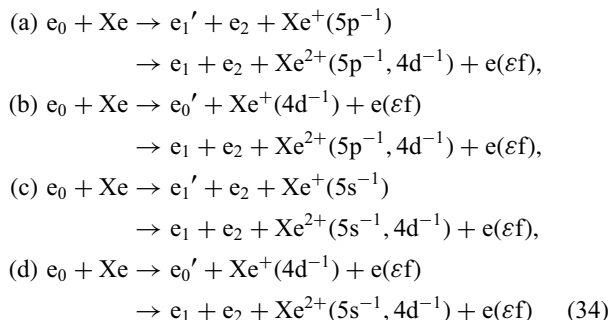
It can be seen from comparison of Figures 16a and 16c that the EMS spectrum, on the whole, is reproduced by the model spectra generated by using the HEPES data, except in the energy region of about 100–140 eV where only EMS exhibits substantial intensity; a great, astonishing difference between EMS and HEPES is observed here. The good agreement between EMS and HEPES in other energy regions suggests that the difference observed here cannot be understood within the first-order approximation such as the DWIA and PWIA. Hence one may conceive that multiple scattering effects and/or higher-order effects are the source of the observed difference. However, results of additional EMS measurements by increasing the ambient sample gas pressure by a factor of 2 have been found to be indistinguishable from the present results,[86] so multiple scattering effects are not the source. Thus, a Gaussian curve centred at $E_{bind} = 120\,eV$ was employed as an additional fitting curve for reproducing the EMS spectrum satisfactorily, as in Figure 17a. Then, a difference spectrum was generated by subtracting the model spectra of the best fit from the EMS spectrum, in order to make the difference between EMS and HEPES directly visible. The result is presented in Figure 17b.

The difference spectrum in Figure 17b clearly reveals the presence of a very broad band (ca. 50 eV FWHM) centred at around 120 eV. The broad nature is strongly reminiscent of giant resonance phenomena,[166] in which the 4d electron is ionized to the f partial wave due to the double well potential. As an example, a spectrum by forward-scattering EELS is included in Figure 17b, which was produced by transforming optical oscillator strength data of Xe[167] using the Bethe–Born formula[3,4] (see eq 1). The giant resonance profile appears as a broad band (ca. 40 eV FWHM) centred at around 100 eV, and its remarkably large cross section can be recognized by comparing the EELS intensity at 100 eV with that at the ionization potential of the 4d electron ($IP_{4d} = $ ca. 69 eV). It is evident from Figure 17b that the difference spectrum is very similar in shape to the EELS spectrum, although the width of the former is about 10 eV larger than that of the latter. Also evident is that the peak of the former is located at about 20 eV higher energy than that of the latter.
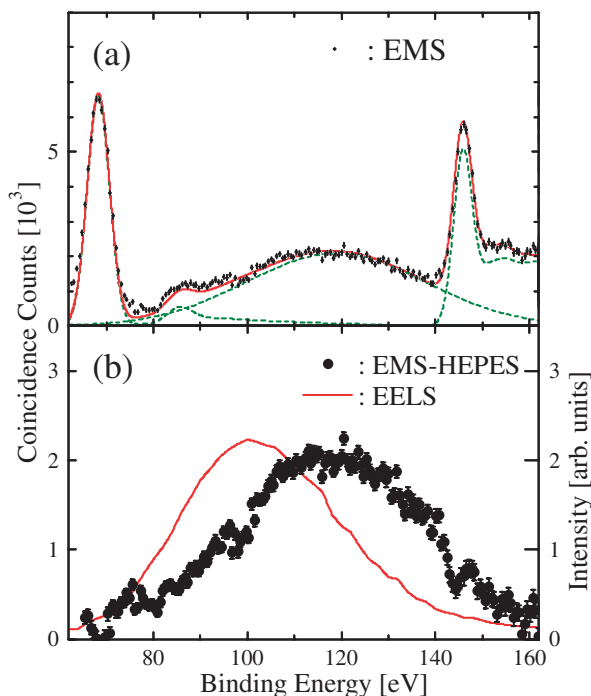
Figure 17. (a) Results of a least-squares fit to the EMS spectrum of Xe in the energy region of 62–162 eV. (b) Difference spectrum which was produced by subtracting the model spectra of the fit from the EMS spectrum. The solid line represents an EELS spectrum, which was generated using the optical oscillator strength of Xe [Ref. 167]. See text for details. Adapted with permission from Ref. 86. Copyright (2007) by the American Physical Society.

The remaining possible source of the difference between EMS and HEPES can give a rational explanation for the observations above, that is, higher-order effects. In particular, the TS mechanisms[153,154] play a critical role here again. They involve two successive half-collisions that lead to a joint change of state of two target electrons, and the following processes can contribute to the EMS spectrum:

(a) $e_0 + Xe \rightarrow e_1' + e_2 + Xe^+(5p^{-1})$
$\qquad \rightarrow e_1 + e_2 + Xe^{2+}(5p^{-1}, 4d^{-1}) + e(\varepsilon f)$,

(b) $e_0 + Xe \rightarrow e_0' + Xe^+(4d^{-1}) + e(\varepsilon f)$
$\qquad \rightarrow e_1 + e_2 + Xe^{2+}(5p^{-1}, 4d^{-1}) + e(\varepsilon f)$,

(c) $e_0 + Xe \rightarrow e_1' + e_2 + Xe^+(5s^{-1})$
$\qquad \rightarrow e_1 + e_2 + Xe^{2+}(5s^{-1}, 4d^{-1}) + e(\varepsilon f)$,

(d) $e_0 + Xe \rightarrow e_0' + Xe^+(4d^{-1}) + e(\varepsilon f)$
$\qquad \rightarrow e_1 + e_2 + Xe^{2+}(5s^{-1}, 4d^{-1}) + e(\varepsilon f)$ (34)

These TS processes consist of the (e,2e) ionization process of the 5p or 5s target electron and the giant resonance process of the 4d electron to εf due to a collision with the incoming or outgoing electron. Overall contributions of the TS processes to the (e,2e) cross section can be expressed by the sum of the two components $|f(5p,4d) + f(4d,5p)|^2 + |f(5s,4d) + f(4d,5s)|^2$, where $f(5p,4d)$, $f(4d,5p)$, $f(5s,4d)$, and $f(4d,5s)$ represent scattering amplitudes of the processes (a), (b), (c), and (d), respectively. The apparent (e,2e) binding energy for the process

(a) [process (b)] is the sum of energy loss in the giant resonance process and ionization transition energy of the 5p electron of Xe [Xe^+ with the 4d hole], i.e., $E_{bind} = E_{gr} + E_{5p}$. The same is true with the processes (c) and (d) if the 5s electron is considered instead of 5p. The giant resonance process involved in the TS processes must be largely dominated by forward scattering under the experimental conditions where energies of all the incident and outgoing electrons are very high compared with the energy loss. In addiiton, photoion yield measurements[158] have shown that the giant resonance profile of Xe^+ is similar in both shape and energy to that of Xe. Hence one can take the peak energy of the EELS spectrum in Figure 17b as a representative of E_{gr}, i.e., $E_{gr} = 100$ eV. Furthermore, for simplicity, let the ionization transition energies of the 5p and 5s electrons of Xe as well as of Xe^+ be the same as transition energies of the $5p^{-1}$ and $5s^{-1}$ main bands of Xe, i.e., $E_{5p} = IP_{5p} =$ ca. 13 and $E_{5s} = IP_{5s} =$ ca. 23 eV. In spite of this rather simple treatment of E_{gr}, E_{5p}, and E_{5s}, one can arrive at a surprisingly good agreement with the observations in Figure 17b. Namely, the two components, $|f(5p,4d) + f(4d,5p)|^2$ and $|f(5s,4d) + f(4d,5s)|^2$, are expected to give contributions centered at $E_{bind} = 113$ and 123 eV to the EMS spectrum, and the average of these values is found very close to the peak energy of the difference spectrum, i.e., $(113 + 123)/2 = 118 \approx 120$ eV. The larger width of the difference spectrum can be qualitatively understood by considering the difference in energy between IP_{5p} and IP_{5s}. Clearly, contributions of the TS processes (a)–(d) can account for the difference between EMS and HEPES. In this way, giant resonance phenomena have been identified, for the first time, in higher-order effects of the projectile-target interaction.

The higher-order effects discussed in Section **5** may not be restricted to electron-impact single ionization as they can occur widely in single- and multiple-ionization processes by impact from any projectile species. For example, one may have the following question; how does a single photon couple to two electrons in the target? This question has been extensively discussed so far in the filed of atomic physics, mostly for photo double ionization (PDI) of the He atom.[168,169] It is generally believed that at the high-energy limit PDI occurs due to the shake-off mechanism, that is, after a sudden removal of one target electron another target electron is ejected as a result of relaxation of the residual ion due to a sudden change in potential. However, at low photon energies, usually employed in chemistry, the TS1 process or the final-state correlation process[170,171] must be certainly possible; one electron absorbs the photon and the resulting photoelectron knocks out the second electron in an (e,2e)-like collision. Apart from the He-atom PDI case, experimental and theoretical studies on higher-order effects for molecules are extremely scarce. There is ample room at this point for chemists to contribute to building up a more complete knowledge about the basic physics and/or the bird's eye view of collisional ionization, which would afford a sound basis for various kinds of spectroscopic methods utilizing ionization phenomena and hence for a wide range of application.

6. Molecular Frame EMS

As has been demonstrated in the preceding sections, EMS is

a very powerful tool for studying electronic structure as well as collision physics. Nevertheless, one may recognize that EMS has not yet reached the stage of full use of its ability for molecules, because the present experiments measure averages over all orientations of gaseous targets. In fact, the spherical averaging results in the enormous loss of versatile information; the intrinsically anisotropic or three-dimensional character of the (e,2e) scattering by molecules deteriorates into the one-dimensional momentum distribution or momentum profile. If it were possible to fix a molecule in space, the experiment would remove ambiguities inherent in the analysis of the spherically averaged (e,2e) cross sections, and further directly provide information important to momentum space chemistry[172–174] as well as to the stereodynamics of electron–molecule collisions.

Indeed, there have been several proposals and even some experiments that seek to measure electron momentum distributions in the three-dimensional form or in the molecular frame. For example, certain molecules adsorbed on metal surfaces take up well defined orientation, but the surface interferes. Laser excitation by polarized light is another means of selecting a population of molecules with a particular orientation. This technique is applicable to atomic targets,[37,175] but cannot be readily applied to molecules because of a large number of rotational states that are populated at room temperature and the narrow band nature of laser light that limits a fraction of molecules in a sample that can be excited. Inhomogeneous strong electric fields are routinely used to orient the angular momentum vectors of rotating molecules. However, the strong fields distort electron trajectories.

There is another opportunity for the investigation. If the molecular ion dissociates much faster than it rotates, the direction of the fragment ion departure coincides with the molecular orientation at the moment of the ionization.[176–178] EMS experiments in conjunction with such axial recoil fragmentation becomes possible only by measurements of vector (energy and angle) correlations between the two outgoing electrons and the fragment ion by a triple coincidence technique, which should be designated as the (e,2e+M) method. Very recently, this type of experiment has been proposed and realized by Takahashi et al.[179,180] In this section, we will see the working principle and details of the (e,2e+M) spectrometer of Takahashi et al. as well as their showcase experiment that has successfully observed molecular frame (e,2e) cross sections for the first time.[179,180]

6.1 Principle. Let us recall the symmetric noncoplanar geometry discussed in Section **2.1**. It is depicted again in Figure 18, together with a pair of entrance apertures (EAs) of a spherical analyzer for determining the acceptance angle of the two outgoing electrons and seven channel-electron-multipliers (CEMs) for detection of the fragment ion. Here the CEMs are placed in the plane ($\theta_M = 90°$) perpendicular to the incident electron momentum vector p_0. The azimuthal angular positions (ϕ_M's) of the CEMs are 0, 45, 90, 150, 195, 240, and 285°.

Although in conventional EMS experiments only the magnitude of the ion recoil momentum vector $|q|$ is a physically important quantity, in the (e,2e+M) experiments the direction of the momentum $q/|q|$ with respect to the molecular axis acquires the central meaning, too. Suppose that the two outgoing electrons at $\theta_1 = \theta_2 = 45°$ are selected by the
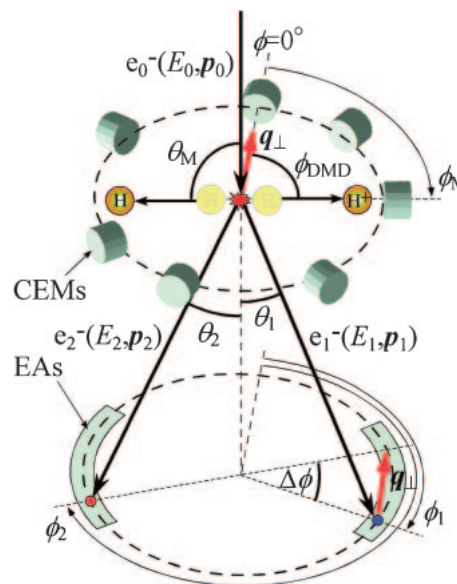

Figure 18. Schematic of an (e,2e+M) experimental setup based on the binary (e,2e) scattering in the symmetric noncoplanar geometry, showing the seven channel-electron-multipliers (CEMs), and a pair of entrance apertures (EAs) of the spherical analyzer followed by a pair of position sensitive detectors. Reproduced with permission from Ref. 180. Copyright (2005) by the American Physical Society.

entrance apertures, which extend over the azimuthal angle ϕ_1 and ϕ_2 ranges from 70 to 110° and from 250 to 290°, as in the (e,2e) spectrometer shown in Figure 4. In this experimental setup, we know that the measured ion recoil momentum q is largely dominated by its component $q_\perp$ perpendicular to p_0. Furthermore, a simulation indicates that the percentage of q's pointing within ±10° from the $\phi = 0$ or 180° directions is about 74%, and that within ±15° is more than 90%. Hence, keeping in mind that the momentum space representation of a target wave function always possesses inversion symmetry [molecular frame (e,2e) cross section within the PWIA $\sigma_{PWIA}(q)$ is equal to $\sigma_{PWIA}(-q)$], the angle ϕ_{DMD} of q from the molecular axis can be approximated as ϕ_M, i.e., $\phi_{DMD} \approx \phi_M$. Thus the experimental setup makes it possible to probe anisotropy or ϕ_{DMD} dependence of the molecular frame (e,2e) cross section in the case of $\theta_M = 90°$. Note that this is enough for constructing momentum density distribution in three-dimensional form when the target is a linear molecule that has rotation symmetry about the molecular axis.

6.2 (e,2e+M) Spectrometer. Figure 19 shows a schematic of the (e,2e+M) spectrometer developed by Takahashi et al.[179] It is placed in a vacuum chamber that is evacuated by a $1500\,dm^3\,s^{-1}$ molecular turbo pump to the base pressure of $2 \times 10^{-5}\,Pa$. The ambient magnetic fields are reduced to lower than $2\,mG$ by double μ-metal shields.

The major sections of the (e,2e+M) spectrometer are an electron gun, a sample inlet system with eight gas-nozzles, a spherical analyzer, two PSDs (RoentDek, DLD40) and seven ion detectors. The present spectrometer is essentially the same as the (e,2e) spectrometer[58] in Figure 4, except for the use of
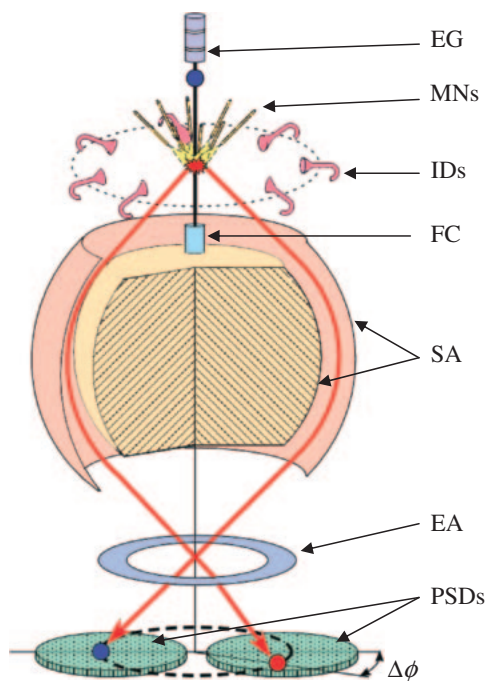
Figure 19. Schematic of an (e,2e+M) spectrometer, showing the electron gun (EG), multi-gas-nozzles (MNs), ion detectors (IDs), Faraday cup (FC), spherical analyzer (SA), exit aperture (EA), and position sensitive detectors (PSDs). Reproduced from Ref. 179.
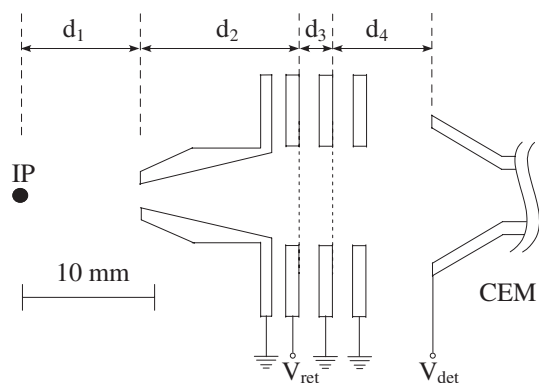
Figure 20. Cross section of the ion detector showing the ionization point (IP) and the channel electron multiplier (CEM). Reproduced from Ref. 179.

the ion detectors. For each of the seven ion detectors a CEM of small size (SJUTS, KBL10RS) is employed to allow close access to the ionization point. The design of the ion detector is shown in Figure 20. The entrance aperture zone is constructed using an aluminium cone. Two copper grids consisting of electroformed mesh (GoodFellow, CU008720) are used to define a retarding electric field for collecting axial recoil fragment ions with large kinetic energies and to produce the ground potential that prevents penetration of the high voltage applied to the CEM into the retarding field, respectively.

Time-of-flight (T) measured for a fragment ion of mass (m) can be converted to the kinetic energy (E_{ion}) from the following relationship:

$$
T_{[ns]} = 102 \times \left[d_{1[mm]} \sqrt{\frac{m_{[amu]}}{2E_{ion[eV]}}} + \int_0^{d_2} dr \sqrt{\frac{m}{2(E_{ion} - eV(r))}} \right.
$$
$$
+ \frac{\sqrt{2m}}{eV_{ret}} d_3 \left(\sqrt{E_{ion}} - \sqrt{E_{ion} - eV_{ret}} \right)
$$
$$
\left. + \frac{\sqrt{2m}}{eV_{det}} d_4 \left(\sqrt{E_{ion} + eV_{det}} - \sqrt{E_{ion}} \right) \right] \tag{35}
$$

Here the d_j's ($j = 1$, 2, 3, and 4) are distances between the ionization point–entrance aperture, entrance aperture–first grid, first grid–second grid, and second grid–CEM, respectively, as defined in Figure 20. V_{ret} and V_{det} are electric voltages applied to the second grid and the CEM. $V(r)$ represents the retarding electric field, which can be estimated using the SIMION program (Idaho National Laboratory). Note that the azimuthal angular positions (ϕ_M's) of the CEMS (0, 45, 90, 150, 195, 240, and 285°) in the perpendicular plane correspond to sampling the molecular frame (e,2e) cross section in full 2π azimuth at 15° intervals in the case of homonuclear diatomic targets, independent of whether or not the PWIA is valid under the experimental conditions employed, because the targets have inversion symmetry and hence $\sigma_{EMS}(q) = \sigma_{EMS}(-q)$. The same is true for heteronuclear targets when the mass resolution is sufficient to separate individual fragment ion species.

A triple coincidence event from the (e,2e+M) spectrometer consists of eleven signals, one originating at one of the seven ion detectors and the others at the two PSDs. Such events are collected with a signal processing electronics system[179] that has been developed based on the electronics system[58] discussed in Section **3.2**. Briefly, a delay time of 500 ns is given to each ion detector signal. The AND function is subsequently applied to the ion detector signals responsible for times-of-flight smaller than 16 μs in order to pick out only those associated with the 400 ns-delayed AND output of the time reference signals. Individual ion detector signals are then merged with one of the delay line signals from the PSDs by the OR function and fed to the seven independent stop channels (1–7) of the TDC.

6.3 (e,2e) Cross Section of Fixed-in-Space Molecules. The show case (e,2e+M) measurements[179,180] have been made for the $2s\sigma_g$ and $2p\sigma_u$ ionization–excitation processes of H_2, under experimental conditions where a retarding voltage (V_{ret}) of 2.5 V and an incident electron energy (E_0) of 1.2 keV have been employed. There are three motivations behind this. First, the two electron system H_2 is the simplest molecule that is always the subject of accurate calculations. Second, since all the transitions to the final excited ion states are followed by direct dissociation, there is no doubt that their fragmentation is largely axial, as demonstrated by photoelectron angular distribution measurements for fixed-in-space H_2 molecules.[181,182] The use of the 2.5 V retarding voltage ensures that energetic fragments H^+ from the excited ion states are detected but those from the $1s\sigma_g$ ground ion state with up to 1 eV kinetic energy as well as the parent ions H_2^+ are entirely removed from the detection.[182–184] Third, it has been found from the EMS study on H_2,[148] discussed in Section **5.1**, that the TS mechanisms play crucial roles in the ionization–excitation processes at $E_0 = 1.2$ keV. Since the TS mechanisms involve two successive half-collisions, their contributions to the (e,2e)

M. Takahashi

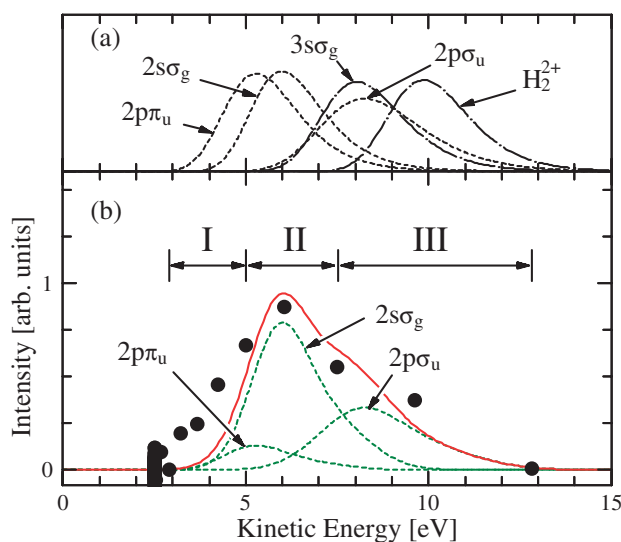*Bull. Chem. Soc. Jpn. Vol. 82, No. 7 (2009)*   771
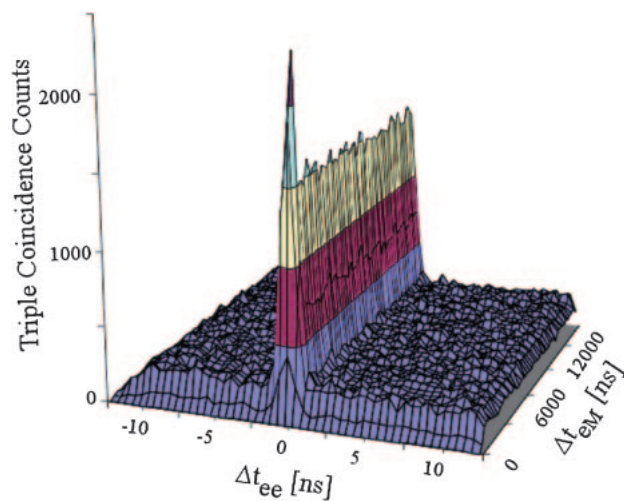
Figure 21. Three-dimensional time spectrum as a function of arrival time difference between the two outgoing electrons Δt_{ee} and that between either of the electrons and the fragment ion Δt_{eM}. Reproduced from Ref. 179.


Figure 22. (a) Calculated kinetic energy distributions of H^+ and (b) observed one. In the lower panel, results of least-squares fit using the theoretical predictions for the $2s\sigma_g$, $2p\sigma_u$, and $2p\pi_u$ transitions are shown by broken lines. The solid line represents their sum. Adapted with permission from Ref. 180. Copyright (2005) by the American Physical Society.

cross section must show stereodynamics in the binary (e,2e) reaction. For instance, the Dunn selection rules[185] about electronic transition by electron impact may work at the excitation processes involved in the TS mechanisms. The (e,2e+M) experiments of H_2 are therefore expected to reveal various kinds of geometry effects in the molecular frame (e,2e) cross section.

As examples of the experimental results,[179,180] let us see first the three-dimensional time spectrum in Figure 21, which represents the number of the triple coincidence events as a function of arrival time difference between the two outgoing electrons Δt_{ee} and that between either of the two electrons and the H^+ fragment Δt_{eM}. Since the three charged particles to be detected are produced in a single event, they must have correlation in their arrival times. Certainly we see the sharp, true (e,2e+M) coincidence peak centred at $\Delta t_{ee} = $ ca. 0 and $\Delta t_{eM} = $ ca. 1×10^3 ns. Substantial background along the $\Delta t_{ee} = 0$ axis is due to accidental coincidence events, in which an uncorrelated fragment ion is detected at nearly the same time while the genuine coincidence detection is made for the two outgoing electrons. Such uncorrelated fragment ions originate mainly from forward scattering of the electron projectile with much larger cross section compared with electron Compton scattering. The background may seem useless but it is potentially useful, because it corresponds to conventional, spherically-averaged (e,2e) data.

Further evidence for the successful measurements is given by examining energy correlation between the two outgoing electrons and the fragment ion. Figure 22a shows theoretical kinetic energy distributions (KEDs) of fragment ions from several of the excited ion states, which were obtained by applying the reflection approximation to the Franck–Condon transition profiles calculated using the BCONT program[152] with the relevant potential energy curves.[151] It can be seen that fragment H^+ ions with kinetic energies larger than about 3 eV are produced from the excited ion states. An experimental KED of H^+ obtained from the true (e,2e+M) coincidence data set is

presented in Figure 22b, which was calculated from the observed times-of-flight of H^+ by using the relationship of eq 35. The experimental result is qualitatively reproduced by a fit (solid line) using the theoretical KEDs (broken lines) for the $2s\sigma_g$, $2p\sigma_u$, and $2p\pi_u$ transitions, the first two of which have been found to be dominant over other ionization–excitation processes at large momentum transfer.[148–150] Thus, the experimental KED was used to check the quality of the (e,2e+M) data, as discussed below.

Initially, the observed kinetic energy range was divided into three regions, as indicated by I, II, and III in Figure 22b. Then (e,2e+M) binding energy spectra were generated by summing the triple coincidence signals over the $\Delta\phi$ and ϕ_M ranges selectively accepting events associated with the H^+ kinetic energy corresponding to the regions I–III, as shown in Figures 23a–23c, respectively. Likewise, a summed (e,2e+M) binding energy spectrum was generated using contributions from the entire kinetic energy range covered, which is also presented in Figure 23d. Here the calculated Franck–Condon transition profiles, after being folded with the instrumental energy resolution, are employed for deconvolution. The best fit to the experimental data are included in the figure.

In Figure 23 we can see results of the energy correlation between the two outgoing electrons and the fragment ion. First, although the (e,2e) cross section for the transition to the $1s\sigma_g$ ground ion state is several tens times larger than those for ionization–excitation transitions, no peak corresponding to the $1s\sigma_g$ transition is observed in the (e,2e+M) spectrum, because of the effect of the retarding potential applied. Traces of the large cross section for the $1s\sigma_g$ transition are left in the relatively large error bars at around 16 eV. Second, since the selection of the H^+ kinetic energy is equivalent to highlighting parts of the Franck–Condon transition profiles of particular
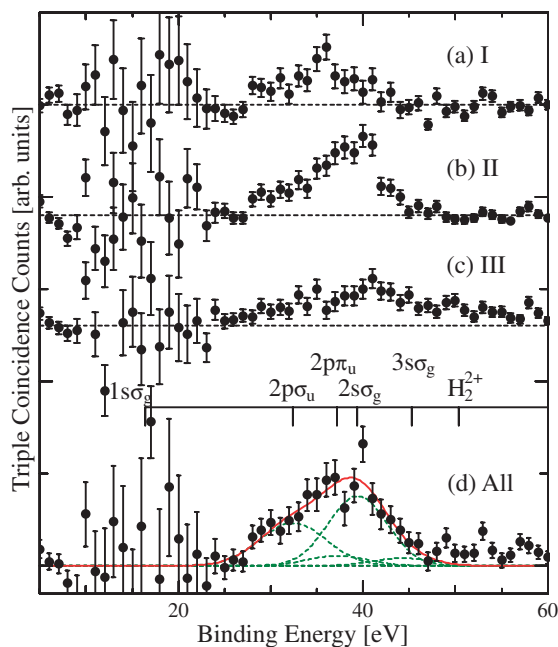
Figure 23. (e,2e+M) binding energy spectra of H_2 associated with the H^+ kinetic energies corresponding to the regions (a) I, (b) II, (c) III, and (d) the entire range defined in Figure 22b. The broken and solid lines in (d) represent the deconvoluted curves and their sum, respectively. Adapted with permission from Ref. 180. Copyright (2005) by the American Physical Society.

transitions, specific ionization–excitation transitions predominate in Figures 23a–23c. The spectrum for selection I exhibits a peak at ca. 36 eV and that for II at ca. 39 eV; these peaks can be ascribed to the $2p\pi_u$ and $2s\sigma_g$ transitions, respectively. Similarly, the spectrum for region III shows a relatively large contribution of the $2p\sigma_u$ transition at ca. 34 eV, together with some contributions from the transitions to $2s\sigma_g$ and higher excited ion states such as $3s\sigma_g$ and H_2^{2+}. These observations confirm that successful measurements of vector correlations among the three charged particles have been achieved and that contributions from individual transitions can be extracted separately by deconvolution as in Figure 23d. A similar fitting procedure was repeated for a series of $\Delta\phi$-angle integrated binding energy spectra at each ϕ_M-angle to produce molecular frame (e,2e) cross sections, summed over the q range covered, for the dominant $2s\sigma_g$ and $2p\sigma_u$ transitions.

The molecular frame (e,2e) cross sections thus obtained for the $2s\sigma_g$ and $2p\sigma_u$ transitions are presented in Figure 24, where they are plotted as a function of ϕ_M or ϕ_{DMD} with the molecular axis drawn in the vertical direction. Here, by taking advantage of the inversion symmetry and rotational symmetry of the molecular frame (e,2e) cross sections about the molecular axis for the homonuclear diatomic molecule H_2, the results are presented so as to give the 24 data points seen, whereas the measurements were performed at only seven ϕ_M's. Distance from the origin to each data point represents the relative magnitude of the cross section obtained at the corresponding ϕ_M-angle. To the best of my knowledge, these are the first observation of (e,2e) cross sections from fixed-in-space molecules.
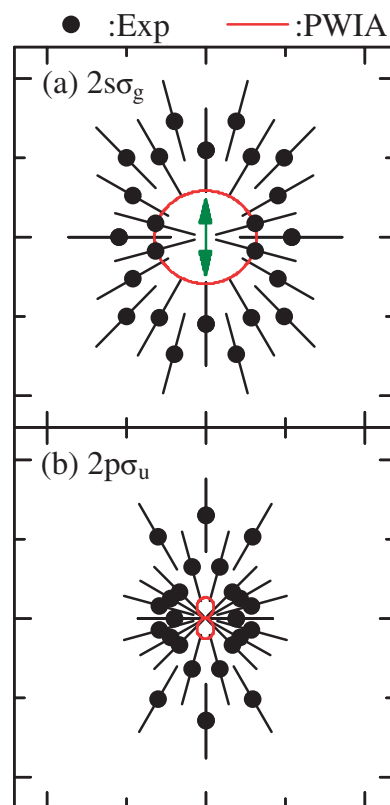
Figure 24. Experimental molecular frame (e,2e) cross sections for H_2 for the transitions to the (a) $2s\sigma_g$ and (b) $2p\sigma_u$ excited ion states, obtained at $E_0 = 1.2\,\text{keV}$. The molecular axis is in the vertical direction. The solid lines represent associated PWIA calculations. Adapted with permission from Ref. 180. Copyright (2005) by the American Physical Society.

Also included in Figure 24 are associated PWIA predictions, shown by solid lines. To place the experiment and theory on a common intensity scale, a normalization procedure[179,180] is used. Briefly, the strengths of the $2s\sigma_g$ and $2p\sigma_u$ transitions relative to the $1s\sigma_g$ transition are maintained in the (e,2e) data, which can be deduced from the present (e,2e+M) data set. Hence the molecular frame (e,2e) cross sections for the $2s\sigma_g$ and $2p\sigma_u$ transitions can be placed on an absolute scale under the assumption that the intensity ratio of the $2s\sigma_g$ experimental and PWIA momentum profiles is valid for the (e,2e+M) $2s\sigma_g$ data. This normalization factor is then applied to the (e,2e+M) $2p\sigma_u$ data. Thus the molecular frame (e,2e) cross sections in Figure 24 share a common intensity scale under the above assumption.

Although the statistics of the experimental results leave much to be desired, anisotropy of the molecular frame (e,2e) cross section and geometry effects of molecular orientation on the (e,2e) scattering amplitudes are evident. Furthermore, we see that the anisotropy of the molecular frame (e,2e) cross section is highly transition-specific. While the angular distribution for the $2s\sigma_g$ transition is relatively isotropic, that for the $2p\sigma_u$ transition shows maxima in the direction of the molecular axis. This is just what the PWIA predicts, because the role of the PWIA in the ionization–excitation processes is to probe

electron momentum densities of the $2s\sigma_g$ and $2p\sigma_u$ excited components involved in the target H_2 wave function. Indeed, the associated PWIA calculations predict such angular distributions which reproduce qualitatively the shapes experimentally observed.

Nevertheless, one may notice in Figure 24 the difference in intensity between the (e,2e+M) and PWIA results. The larger difference observed in the $2p\sigma_u$ channel than that in the $2s\sigma_g$ channel is consistent with the findings of the EMS study on H_2.[148] Thus the $2p\sigma_u$ results may particularly offer one an opportunity to study geometry effects of molecular orientation in the TS mechanisms, because the extent of the intensity difference between the (e,2e+M) and PWIA result is a rough measure of contributions of the TS mechanisms. Interestingly, the $2p\sigma_u$ experiments appear to show more significant deviation from the PWIA in the direction of the molecular axis. If this observation is real, it would indicate that the two outgoing electrons escape preferentially so as to leave the ion recoil momentum vector q in the direction of the molecular axis. In other words, roughly speaking, the binary (e,2e) reaction with the higher-order interactions favors molecular orientation perpendicular to the scattering plane, defined by p_0 and p_1, rather than parallel. However, we have to leave a full discussion of it for a later publication with improved data, because the poor statistics of the present data make it difficult to discuss such geometry effects fruitfully. Another promising direction may be to perform similar (e,2e+M) experiments on various linear molecules, at higher incident electron energies where the (e,2e) reaction approaches more and more the high-energy limit and hence the momentum space representation of molecular orbitals can be imaged more quantitatively in three-dimensional form. Very recently, (e,2e+M) experiments on H_2 at a higher incident electron energy of 2.0 keV have been carried out by Shibuya et al.,[186] in which molecular frame (e,2e) cross sections for the $2s\sigma_g$ and $2p\sigma_u$ transitions have been obtained with much improved statistical uncertainties. The more accurate observations on the molecular orbital patterns will be reported.[186] On the other hand, Takahashi and Udagawa[187] have pointed out that molecular frame (e,2e) cross sections can be measured as a function of the nuclear separation length in addition to the magnitude and direction of the momentum vector q, by making full use of the information obtainable from vector correlations between the two outgoing electrons and the fragment ion. Further attempts along these lines would develop unexploited possibilities of electron Compton scattering, opening the door for detailed studies of bound electron wave functions of molecules as well as those of stereodynamics of electron-molecule collisions.

7. Concluding Remarks

In this account I have reviewed the expanding frontiers of EMS in multichannel techniques, electronic structure studies with one-electron and two-electron processes, and molecular frame measurements. It is largely because of the historical devotion of many researchers since the pioneering work of Amaldi et al.,[17] Camilloni et al.,[18] and Weigold et al.[19] that the frontiers have been opened up. Nevertheless, I would boldly declare that EMS is still in its infancy, as may be apparent from

the discussions in the preceding sections; EMS is a method of great capabilities. In this respect, the following four areas are suggested for future efforts.

First, developments of multichannel techniques are to be advanced further. By reminding us that a significant portion (ca. 99%) of available signal is wasted even with the latest techniques[58,59] as noted in Section **3**, such further developments are crucial in order to unlock and make full use of uncharted abilities of EMS for a variety of fields in chemistry. For instance, one will be able to make radicals and ions to be the targets in the near future. As well, vibrationally-resolved EMS experiments will become possible by improving the energy resolution that has always been in a trade-off with the signal count rate.

Second, developments of theoretical methods are also crucial; indeed, electron Compton scattering or (e,2e) reaction dynamics at large momentum transfer generally has not been satisfactorily analyzed. For example, calculations by using the distorted wave theory are eagerly awaited for various molecules including O_2,[102] CH_3OH,[188] C_2H_4,[104,105] C_2H_6,[106] glyoxal and biacetyl,[64] and $Cr(CO)_6$, $Mo(CO)_6$, and $W(CO)_6$.[189] Even though such perturbative approach[1,2,153,154,190] may not finally turn out to be the best way of predicting how the (e,2e) reaction dynamics varies from the intermediate regime to the high-energy regime, the view will long continue to yield important insights into electron Compton scattering, as demonstrated in Section **5**. Furthermore, agreement between experiment and theory does not necessarily prove that the theoretical model employed is correct; however, disagreement proves absolutely that it is wrong. Hence, organized efforts of theory and experiment will be necessary in this respect. Achieving a more complete knowledge of the range of validity of the PWIA is one of the vital issues hereupon. Additionally, comparative studies of electron (e^-) and positron (e^+) scattering would be interesting, because they can illuminate exchange and polarization effects that depend on the electron–electron interaction during the (e,2e) collision.

Third, the present (e,2e+M) method[179,180] is to be advanced. Although it has pioneered molecular frame EMS, there is ample room for improvements mainly in collection efficiency, which could be achieved by the detection of the two outgoing electrons in the momentum dispersive plane around the full 2π azimuth and detection of the fragment ion over the full 4π solid angle. These attempts work not only as the way to improve rather poor statistics of the present (e,2e+M) measurements but also as the key to extending the applicability of the method, i.e., the monopolistic power to image momentum space representation of molecular orbitals in three-dimensional form, from linear molecules to a variety of molecules. A related topic is stereodynamics of electron–molecule collisions, for which all possible molecular orientations with respect to the incident electron momentum vector should be examined while a wide range of momentum transfer from zero to a large value is covered. This would serve as a clue for taking a bird's-eye view over the physics of electron–molecule collision from the dipole regime to the Compton regime continuously.

Fourthly, a quantum leap in experimental techniques would be desired, which introduces the pump-and-probe technique into electron Compton scattering experiments: developments

of the time-resolved (e,2e+M) method or the time-resolved reaction microscope for electron Compton scattering. Here the inelastically scattered electron, ejected electron, and fragment ion produced by Compton scattering in the collision of a pulsed electron beam with a transient species, that is prepared beforehand with a pump pulse laser, are measured in coincidence, whilst the timing of the ionization with respect to the pump pulse is varied. The experimental data of vector correlations amongst the three charged particles are subsequently employed to construct the electron momentum distribution functions of the transient species as a function of electron binding energy in addition to the timing of the ionization. This new method may be unique in its ability to visualize the change of electron motion in a transient or intermediate species, which is the driving force behind any chemical reaction. If the method will be successfully developed, it represents the first time that the change of electron motion in matter would become observable, thus exploring previously uncharted areas of photoinduced ultrafast dynamics[191] such as excitation-energy transfer, electron transfer and isomerisation processes. My group has just launched this challenging project, with which qualitative changes could be brought about eventually into the understanding of chemical bonding and chemical reactions and hence its outcome is expected to have a profound impact upon a wide range of fields from material science to life science. Recent developments of the pulsed electron beam techniques (temporal resolution of a few hundred fs)[192] are encouraging in this respect. I hope that the time-resolved (e,2e+M) method and other techniques, such as the tomographic imaging method[193] using high harmonic generation in an intense laser field, will be able to serve as popular means to see how the electron wave function evolves as time advances in momentum space and position space, respectively.

References

1   M. Born, *Z. Phys.* **1926**, *38*, 803.

2   H. Bethe, *Ann. Phys.* **1930**, *397*, 325.

3   M. Inokuti, *Rev. Mod. Phys.* **1971**, *43*, 297.

4   R. A. Bonham, M. Fink, *High Energy Electron Scattering*, Van Nostrand Reinhold, New York, **1974**.

5   M. Takahashi, N. Watanabe, Y. Wada, S. Tsuchizawa, T. Hirosue, H. Hayashi, Y. Udagawa, *J. Electron Spectrosc. Relat. Phenom.* **2000**, *112*, 107.

6   E. N. Lassettre, *J. Chem. Phys.* **1965**, *43*, 4479.

7   *Compton Scattering*, ed. by B. Williams, McGraw-Hill, New York, **1977**.

8   A. L. Hughes, M. M. Mann, Jr., *Phys. Rev.* **1938**, *53*, 50.

9   A. L. Hughes, M. A. Starr, *Phys. Rev.* **1938**, *54*, 189.

10   A. L. Hughes, M. A. Starr, *Phys. Rev.* **1939**, *55*, 343.

11   A. L. Hughes, T. Enns, *Phys. Rev.* **1941**, *60*, 345.

12   G. A. Baker, Jr., I. E. McCarthy, C. E. Porter, *Phys. Rev.* **1960**, *120*, 254.

13   I. E. McCarthy, E. V. Jezak, A. J. Kromminga, *Nucl. Phys.* **1959**, *12*, 274.

14   Yu. F. Smirnov, V. G. Neudatchin, *Pis'ma Zh. Eksp. Teor. Fiz.* **1966**, *3*, 298.

15   Yu. F. Smirnov, V. G. Neudatchin, *JETP Lett.* **1966**, *3*, 192.

16   The reaction can be written in nuclear physicist's notation as $M(e,2e)M^+$, where the reactants are to the left of the comma while the products are on the right hand side. The equation corresponds to the more familiar chemist's notation: $M + e^- \rightarrow e^- + e^- + M^+$.

17   U. Amaldi, Jr., A. Egidi, R. Marconero, G. Pizzella, *Rev. Sci. Instrum.* **1969**, *40*, 1001.

18   R. Camilloni, A. Giardini-Guidoni, R. Tiribelli, G. Stefani, *Phys. Rev. Lett.* **1972**, *29*, 618.

19   E. Weigold, S. T. Hood, P. J. O. Teubner, *Phys. Rev. Lett.* **1973**, *30*, 475.

20   B. Lohmann, E. Weigold, *Phys. Lett.* **1981**, *86A*, 139.

21   S. Dey, I. E. McCarthy, P. J. O. Teubner, E. Weigold, *Phys. Rev. Lett.* **1975**, *34*, 782.

22   S. T. Hood, A. Hamnett, C. E. Brion, *Chem. Phys. Lett.* **1976**, *39*, 252.

23   A. O. Bawagan, C. E. Brion, E. R. Davidson, D. Feller, *Chem. Phys.* **1987**, *113*, 19.

24   S. W. Braidwood, M. J. Brunger, D. A. Konovalov, E. Weigold, *J. Phys. B: At., Mol. Opt. Phys.* **1993**, *26*, 1655.

25   E. Weigold, K. Zhao, W. von Niessen, *J. Chem. Phys.* **1991**, *94*, 3468.

26   J. Rolke, Y. Zheng, C. E. Brion, Y. A. Wang, E. R. Davidson, *Chem. Phys.* **1998**, *230*, 153.

27   M. Takahashi, K. Otsuka, Y. Udagawa, *Chem. Phys.* **1998**, *227*, 375.

28   M. J. Brunger, I. E. McCarthy, E. Weigold, *Phys. Rev. A* **1999**, *59*, 1245.

29   M. Takahashi, R. Ogino, Y. Udagawa, *Chem. Phys. Lett.* **1998**, *288*, 714.

30   M. Takahashi, M. Matsuo, Y. Udagawa, *Chem. Phys. Lett.* **1999**, *308*, 195.

31   J. A. Tossell, J. H. Moore, M. A. Coplan, G. Stefani, R. Camilloni, *J. Am. Chem. Soc.* **1982**, *104*, 7416.

32   J. A. Tossell, S. M. Lederman, J. H. Moore, M. A. Coplan, D. J. Chornay, *J. Am. Chem. Soc.* **1984**, *106*, 976.

33   R. R. Goruganthu, M. A. Coplan, J. H. Moore, J. A. Tossell, *J. Chem. Phys.* **1988**, *89*, 25.

34   J. P. D. Cook, J. Mitroy, E. Weigold, *Phys. Rev. Lett.* **1984**, *52*, 1116.

35   J. P. D. Cook, I. E. McCarthy, J. Mitroy, E. Weigold, *Phys. Rev. A* **1986**, *33*, 211.

36   L. Frost, J. Mitroy, E. Weigold, *J. Phys. B: At., Mol. Phys.* **1986**, *19*, 4063.

37   Y. Zheng, I. E. McCarthy, E. Weigold, D. Zhang, *Phys. Rev. Lett.* **1990**, *64*, 1358.

38   K. McMillan, M. A. Coplan, J. H. Moore, J. A. Tossell, *J. Phys. Chem.* **1990**, *94*, 8648.

39   J. H. Moore, M. A. Coplan, T. L. Skillman, Jr., E. D. Brooks, III, *Rev. Sci. Instrum.* **1978**, *49*, 463.

40   I. E. McCarthy, E. Weigold, *Phys. Rev. A* **1985**, *31*, 160.

41   B. R. Todd, N. Lermer, C. E. Brion, *Rev. Sci. Instrum.* **1994**, *65*, 349.

42   Y. Zheng, J. J. Neville, C. E. Brion, Y. Wang, E. R. Davidson, *Chem. Phys.* **1994**, *188*, 109.

43   M. Takahashi, H. Nagasaka, Y. Udagawa, *J. Phys. Chem. A* **1997**, *101*, 528.

44   Y. Zheng, G. Cooper, S. Tixier, B. R. Todd, C. E. Brion, *J. Electron Spectrosc. Relat. Phenom.* **2000**, *112*, 67.

45   I. E. McCarthy, E. Weigold, *Phys. Rep.* **1976**, *27*, 275.

46   C. E. Brion, *Int. J. Quantum Chem.* **1986**, *29*, 1397.

47   K. T. Leung, in *Theoretical Models of Chemical Bonding*, Part 3, ed. by Z. B. Maksic, Springer-Verlag, Berlin, **1991**, pp. 339–386.

48   I. E. McCarthy, E. Weigold, *Rep. Prog. Phys.* **1991**, *54*, 789.

49   M. A. Coplan, J. H. Moore, J. A. Tossell, *Z. Naturforsch.* **1993**, *48a*, 358.

50   E. Weigold, *Z. Naturforsch.* **1993**, *48a*, 371.

51   M. A. Coplan, J. H. Moore, J. P. Doering, *Rev. Mod. Phys.* **1994**, *66*, 985.

52   V. G. Neudachin, Y. V. Popov, Y. F. Smirnov, *Phys. Usp.* **1999**, *42*, 1017.

53   E. Weigold, I. E. McCarthy, *Electron Momentum Spectroscopy*, Kluwer Academic/Plenum Publishers, New York, **1999**.

54   C. E. Brion, G. Cooper, Y. Zheng, I. V. Litvinyuk, I. E. McCarthy, *Chem. Phys.* **2001**, *270*, 13.

55   I. E. McCarthy, E. Weigold, *Rep. Prog. Phys.* **1988**, *51*, 299.

56   W. F. Ford, *Phys. Rev.* **1964**, *133*, B1616.

57   J. H. Moore, C. C. Davis, M. A. Coplan, S. Greer, *Building Scientific Apparatus*, 3rd ed., Westview Press, **2002**.

58   M. Takahashi, T. Saito, M. Matsuo, Y. Udagawa, *Rev. Sci. Instrum.* **2002**, *73*, 2242.

59   X. G. Ren, C. G. Ning, J. K. Deng, S. F. Zhang, G. L. Su, F. Huang, G. Q. Li, *Rev. Sci. Instrum.* **2005**, *76*, 063103.

60   E. M. Purcell, *Phys. Rev.* **1938**, *54*, 818.

61   R. Herzog, *Z. Phys.* **1935**, *97*, 596.

62   E. Harting, F. H. Read, *Electrostatic Lenses*, Elsevier, Amsterdam, **1976**.

63   Y. Miyake, M. Takahashi, N. Watanabe, Y. Khajuria, Y. Udagawa, Y. Sakai, T. Mukoyama, *Phys. Chem. Chem. Phys.* **2006**, *8*, 3022.

64   M. Takahashi, T. Saito, J. Hiraka, Y. Udagawa, *J. Phys. B: At., Mol. Opt. Phys.* **2003**, *36*, 2539.

65   S. T. Hood, I. E. McCarthy, P. J. O. Teubner, E. Weigold, *Phys. Rev. A* **1973**, *8*, 2494.

66   K. T. Leung, C. E. Brion, *Chem. Phys.* **1983**, *82*, 87.

67   K. T. Leung, C. E. Brion, *Chem. Phys.* **1983**, *82*, 113.

68   J. P. D. Cook, I. E. McCarthy, A. T. Stelbovics, E. Weigold, *J. Phys. B: At., Mol. Opt. Phys.* **1984**, *17*, 2339.

69   A. D. Smith, M. A. Coplan, D. J. Chornay, J. H. Moore, J. A. Tossell, J. Mrozek, V. H. Smith, Jr., N. S. Chant, *J. Phys. B: At., Mol. Opt. Phys.* **1986**, *19*, 969.

70   I. E. McCarthy, J. Mitroy, *Phys. Rev. A* **1986**, *34*, 4426.

71   N. Lermer, B. R. Todd, N. M. Cann, C. E. Brion, Y. Zheng, S. Chakravorty, E. R. Davidson, *Can. J. Phys.* **1996**, *74*, 748.

72   N. Watanabe, Y. Khajuria, M. Takahashi, Y. Udagawa, P. S. Vinitsky, Y. V. Popov, O. Chuluunbaatar, K. A. Kouzakov, *Phys. Rev. A* **2005**, *72*, 032705.

73   X. G. Ren, C. G. Ning, J. K. Deng, G. L. Su, S. F. Zhang, Y. R. Huang, G. Q. Li, *Phys. Rev. A* **2005**, *72*, 042718.

74   N. Watanabe, M. Takahashi, Y. Udagawa, K. A. Kouzakov, Y. V. Popov, *Phys. Rev. A* **2007**, *75*, 052701.

75   O. Samardzic, S. W. Braidwood, E. Weigold, M. J. Brunger, *Phys. Rev. A* **1993**, *48*, 4390.

76   N. Watanabe, Y. Khajuria, M. Takahashi, Y. Udagawa, *J. Electron Spectrosc. Relat. Phenom.* **2005**, *142*, 325.

77   S. T. Hood, I. E. McCarthy, P. J. O. Teubner, E. Weigold, *Phys. Rev. A* **1974**, *9*, 260.

78   E. Weigold, I. E. McCarthy, *Adv. At. Mol. Phys.* **1978**, *14*, 127.

79   I. E. McCarthy, R. Pascual, P. Storer, E. Weigold, *Phys. Rev. A* **1989**, *40*, 3041.

80   A. S. Kheifets, M. Vos, E. Weigold, M. J. Brunger, I. E. McCarthy, *Phys. Rev. A* **1998**, *58*, 2815.

81   R. Nicholson, S. Braidwood, I. E. McCarthy, E. Weigold, M. J. Brunger, *Phys. Rev. A* **1996**, *53*, 4205.

82   S. Braidwood, M. Brunger, E. Weigold, *Phys. Rev. A* **1993**, *47*, 2927.

83   M. J. Brunger, S. W. Braidwood, I. E. McCarthy, E. Weigold, *J. Phys. B: At., Mol. Opt. Phys.* **1994**, *27*, L597.

84   C. E. Brion, Y. Zheng, J. Rolke, J. J. Neville, I. E. McCarthy, J. Wang, *J. Phys. B: At., Mol. Opt. Phys.* **1998**, *31*, L223.

85   X. G. Ren, C. G. Ning, J. K. Deng, G. L. Su, S. F. Zhang, Y. R. Huang, *Phys. Rev. A* **2006**, *73*, 042714.

86   M. Takahashi, Y. Miyake, N. Watanabe, Y. Udagawa, Y. Sakai, T. Mukoyama, *Phys. Rev. Lett.* **2007**, *98*, 013201.

87   K. G. Dyall, F. P. Larkins, *J. Phys. B: At., Mol. Opt. Phys.* **1982**, *15*, 219.

88   R. Hoffmann, A. Imamura, W. J. Hehre, *J. Am. Chem. Soc.* **1968**, *90*, 1499.

89   R. Hoffmann, *Acc. Chem. Res.* **1971**, *4*, 1.

90   J. L. Wiza, *Nucl. Instrum. Methods* **1979**, *162*, 587.

91   R. R. Goruganthu, W. G. Wilson, *Rev. Sci. Instrum.* **1984**, *55*, 2030.

92   C. E. Brion, I. E. McCarthy, I. H. Suzuki, E. Weigold, *Chem. Phys. Lett.* **1979**, *67*, 115.

93   C. E. Brion, S. T. Hood, I. H. Suzuki, E. Weigold, G. R. J. Williams, *J. Electron Spectrosc. Relat. Phenom.* **1980**, *21*, 71.

94   S. Dey, A. J. Dixson, K. R. Lassey, I. E. McCarthy, P. J. O. Teubner, E. Weigold, P. S. Bagus, E. K. Viinikka, *Phys. Rev. A* **1977**, *15*, 102.

95   H. Mackenzie-Ross, M. J. Brunger, F. Wang, W. Adcock, N. Trout, I. E. McCarthy, D. A. Winkler, *J. Electron Spectrosc. Relat. Phenom.* **2002**, *123*, 389.

96   P. Duffy, D. P. Chong, M. E. Casida, D. R. Salahub, *Phys. Rev. A* **1994**, *50*, 4707.

97   M. E. Casida, *Phys. Rev. A* **1995**, *51*, 2005.

98   P. Duffy, *Can. J. Phys.* **1996**, *74*, 763.

99   W. Kohn, L. J. Sham, *Phys. Rev.* **1965**, *140*, A1133.

100   A. O. Bawagan, L. Y. Lee, K. T. Leung, C. E. Brion, *Chem. Phys.* **1985**, *99*, 367.

101   A. O. Bawagan, C. E. Brion, *Chem. Phys.* **1988**, *123*, 51.

102   C. G. Ning, X. G. Ren, J. K. Deng, G. L. Su, S. F. Zhang, G. Q. Li, *Phys. Rev. A* **2006**, *73*, 022704.

103   Y. Khajuria, M. Takahashi, Y. Udagawa, *J. Electron Spectrosc. Relat. Phenom.* **2003**, *133*, 113.

104   X. G. Ren, C. G. Ning, J. K. Deng, S. F. Zhang, G. L. Su, F. Huang, G. Q. Li, *Phys. Rev. Lett.* **2005**, *94*, 163201.

105   X. G. Ren, C. G. Ning, J. K. Deng, S. F. Zhang, G. L. Su, F. Huang, G. Q. Li, *Chem. Phys. Lett.* **2005**, *404*, 279.

106   X. G. Ren, C. G. Ning, J. K. Deng, S. F. Zhang, G. L. Su, Y. R. Huang, G. Q. Li, *J. Electron Spectrosc. Relat. Phenom.* **2006**, *151*, 92.

107   T. A. Carlson, *Phys. Rev.* **1967**, *156*, 142.

108   J. Schirmer, L. S. Cederbaum, O. Walter, *Phys. Rev. A* **1983**, *28*, 1237.

109   J. Schirmer, G. Angonoa, *J. Chem. Phys.* **1989**, *91*, 1754.

110   H.-G. Weikert, H.-D. Meyer, L. S. Cederbaum, F. Tarantelli, *J. Chem. Phys.* **1996**, *104*, 7122.

111   M. S. Deleuze, M. G. Giuffreda, J.-P. François, L. S. Cederbaum, *J. Chem. Phys.* **1999**, *111*, 5851.

112   H. Nakatsuji, *Chem. Phys. Lett.* **1978**, *59*, 362.

113   H. Nakatsuji, *Chem. Phys. Lett.* **1979**, *67*, 329.

114   H. Nakatsuji, *Chem. Phys. Lett.* **1979**, *67*, 334.

115   H. Nakatsuji, *Chem. Phys.* **1983**, *75*, 425.

116   H. Nakatsuji, *Computational Chemistry—Review of Current Trends*, Vol. 2, World Scientific, Singapore, **1997**, p. 62.

117   F. Wang, H. Mackenzie-Ross, D. A. Winkler, I. E. McCarthy, L. Campbell, M. J. Brunger, *J. Comput. Chem.* **2001**, *22*, 1321.

118   F. Wang, M. J. Brunger, F. P. Larkins, *J. Phys. Chem. A* **2001**, *105*, 1254.

119   S. Tixier, W. A. Shapley, Y. Zheng, D. P. Chong, C. E. Brion, Z. Shi, S. Wolfe, *Chem. Phys.* **2001**, *270*, 263.

120   Y. Zheng, J. Rolke, G. Cooper, C. E. Brion, *J. Electron Spectrosc. Relat. Phenom.* **2002**, *123*, 377.

121   G. L. Su, X. G. Ren, S. F. Zhang, C. G. Ning, H. Zhou, B. Li, G. Q. Li, J. K. Deng, Y. Wang, Y. Zheng, *Chem. Phys. Lett.* **2004**, *385*, 498.

122   G. Q. Li, J. K. Deng, B. Li, X. G. Ren, C. G. Ning, *Phys. Rev. A* **2005**, *72*, 062716.

123   J. K. Deng, G. Q. Li, Y. He, J. D. Huang, H. Deng, X. D. Wang, F. Wang, Y. A. Zhang, C. G. Ning, N. F. Gao, Y. Wang, X. J. Chen, Y. Zheng, *J. Chem. Phys.* **2001**, *114*, 882.

124   J. K. Deng, G. Q. Li, X. D. Wang, J. D. Huang, H. Deng, C. G. Ning, Y. Wang, *J. Chem. Phys.* **2002**, *117*, 4839.

125   J. K. Deng, G. Q. Li, F. Wang, G. L. Su, C. G. Ning, T. Zhang, X. G. Ren, Y. Wang, Y. Zheng, *J. Chem. Phys.* **2004**, *120*, 10009.

126   X. G. Ren, C. G. Ning, S. F. Zhang, G. L. Su, B. Li, H. Zhou, Y. R. Huang, G. Q. Li, J. K. Deng, *J. Electron Spectrosc. Relat. Phenom.* **2005**, *149*, 29.

127   C. G. Ning, X. G. Ren, J. K. Deng, S. F. Zhang, G. L. Su, F. Huang, G. Q. Li, *J. Chem. Phys.* **2005**, *122*, 224302.

128   S. Saha, F. Wang, C. T. Falzon, M. J. Brunger, *J. Chem. Phys.* **2005**, *123*, 124315.

129   M. S. Deleuze, S. Knippenberg, *J. Chem. Phys.* **2006**, *125*, 104309.

130   X. J. Chen, C. K. Xu, C. C. Jia, Y. Khajuria, K. Z. Xu, *J. Phys. B: At., Mol. Opt. Phys.* **2001**, *34*, 4845.

131   G. L. Su, C. G. Ning, S. F. Zhang, X. G. Ren, H. Zhou, B. Li, F. Huang, G. Q. Li, J. K. Deng, *J. Chem. Phys.* **2005**, *122*, 054301.

132   X. J. Chen, L. X. Zhou, X. H. Zhang, X. F. Yin, C. K. Xu, X. Shan, Z. Wei, K. Z. Xu, *J. Chem. Phys.* **2004**, *120*, 7933.

133   L. X. Zhou, X. Shan, X. J. Chen, X. F. Yin, X. H. Zhang, C. K. Xu, Z. Wei, K. Z. Xu, *J. Electron Spectrosc. Relat. Phenom.* **2006**, *153*, 58.

134   C. G. Ning, X. G. Ren, J. K. Deng, G. L. Su, S. F. Zhang, S. Knippenberg, M. S. Deleuze, *Chem. Phys. Lett.* **2006**, *421*, 52.

135   X. Shan, X. J. Chen, C. K. Xu, L. X. Zhou, K. Z. Xu, *Chem. Phys. Lett.* **2006**, *422*, 246.

136   M. Takahashi, R. Ogino, Y. Udagawa, *Chem. Phys. Lett.* **1998**, *288*, 821.

137   S. F. Zhang, X. G. Ren, G. L. Su, C. G. Ning, H. Zhou, B. Li, F. Huang, G. Q. Li, J. K. Deng, *Chem. Phys. Lett.* **2005**, *401*, 80.

138   M. Ehara, Y. Ohtsuka, H. Nakatsuji, M. Takahashi, Y. Udagawa, *J. Chem. Phys.* **2005**, *122*, 234319.

139   H. Mackenzie-Ross, M. J. Brunger, F. Wang, W. Adcock, T. Maddern, L. Campbell, W. R. Newell, I. E. McCarthy, E. Weigold, B. Appelbe, D. A. Winkler, *J. Phys. Chem. A* **2002**, *106*, 9573.

140   K. L. Nixon, F. Wang, L. Campbell, T. Maddern, D. Winkler, R. Gleiter, P. Loeb, E. Weigold, M. J. Brunger, *J. Phys. B: At., Mol. Opt. Phys.* **2003**, *36*, 3155.

141   F. Wang, M. J. Brunger, I. E. McCarthy, D. A. Winkler, *Chem. Phys. Lett.* **2003**, *382*, 217.

142   S. Knippenberg, K. L. Nixon, M. J. Brunger, T. Maddern, L. Campbell, N. Trout, F. Wang, W. R. Newell, M. S. Deleuze, J.-P. François, D. A. Winkler, *J. Chem. Phys.* **2004**, *121*, 10525.

143   S. Knippenberg, K. L. Nixon, H. Mackenzie-Ross, M. J. Brunger, F. Wang, M. S. Deleuze, J.-P. François, D. A. Winkler, *J. Phys. Chem. A* **2005**, *109*, 9324.

144   D. B. Jones, M. A. Bolorizadeh, M. J. Brunger, S. Saha, F. Wang, R. Gleiter, J. Bueber, D. A. Winkler, *J. Phys. B: At., Mol. Opt. Phys.* **2006**, *39*, 2411.

145   S. Knippenberg, J.-P. François, M. S. Deleuze, *J. Comput. Chem.* **2006**, *27*, 1703.

146   I. V. Litvinyuk, J. B. Young, Y. Zheng, G. Cooper, C. E. Brion, *Chem. Phys.* **2001**, *263*, 195.

147   D. B. Jones, F. Wang, D. A. Winkler, M. J. Brunger, *Biophys. Chem.* **2006**, *121*, 105.

148   M. Takahashi, Y. Khajuria, Y. Udagawa, *Phys. Rev. A* **2003**, *68*, 042710.

149   E. Weigold, I. E. McCarthy, A. J. Dixson, S. Dey, *Chem. Phys. Lett.* **1977**, *47*, 209.

150   N. Lermer, B. R. Todd, N. M. Cann, Y. Zheng, C. E. Brion, Z. Yang, E. R. Davidson, *Phys. Rev. A* **1997**, *56*, 1393.

151   T. E. Sharp, *At. Data Nucl. Data Tables* **1970**, *2*, 119.

152   R. J. Le Roy, *Comput. Phys. Commun.* **1989**, *52*, 383.

153   T. A. Carlson, M. O. Krause, *Phys. Rev.* **1965**, *140*, A1057.

154   R. J. Tweed, *Z. Phys. D: At., Mol. Clusters* **1992**, *23*, 309.

155   E. W. B. Dias, H. S. Chakraborty, P. C. Deshmukh, S. T. Manson, O. Hemmers, P. Glans, D. L. Hansen, H. Wang, S. B. Whitfield, D. W. Lindle, R. Wehlitz, J. C. Levin, I. A. Sellin, R. C. C. Perera, *Phys. Rev. Lett.* **1997**, *78*, 4553.

156   Y. Asano, N. Watanabe, M. Takahashi, to be submitted.

157   N. Watanabe, M. Takahashi, to be submitted.

158   M. Sano, Y. Itoh, T. Koizumi, T. M. Kojima, S. D. Kravis, M. Oura, T. Sekioka, N. Watanabe, Y. Awaya, F. Koike, *J. Phys. B: At., Mol. Opt. Phys.* **1996**, *29*, 5305.

159   B.-S. Min, Y. Yoshinari, T. Watabe, Y. Tanaka, C. Takayanagi, T. Takayanagi, K. Wakiya, H. Suzuki, *J. Phys. Soc.*

Jpn. **1993**, *62*, 1183.

160 G. Laricchia, P. van Reeth, M. Szluinska, J. Moxom, *J. Phys. B: At., Mol. Opt. Phys.* **2002**, *35*, 2525.

161 U. Gelius, *J. Electron Spectrosc. Relat. Phenom.* **1974**, *5*, 985.

162 S. Svensson, B. Eriksson, N. Mårtensson, G. Wendin, U. Gelius, *J. Electron Spectrosc. Relat. Phenom.* **1988**, *47*, 327.

163 A. S. Kheifets, M. Y. Amusia, *Phys. Rev. A* **1992**, *46*, 1261.

164 T. Åberg, *Phys. Lett. A* **1968**, *26*, 515.

165 R. L. Martin, D. A. Shirley, *Phys. Rev. A* **1976**, *13*, 1475.

166 J. P. Connerade, J. M. Esteva, R. C. Karnatak, *Giant Resonance in Atoms, Molecules, and Solids*, Plenum, New York, **1986**.

167 W. F. Chan, G. Cooper, X. Guo, G. R. Burton, C. E. Brion, *Phys. Rev. A* **1992**, *46*, 149.

168 J. H. McGuire, N. Berrah, R. J. Bartlett, J. A. R. Samson, J. A. Tanis, C. L. Cocke, A. S. Schlachter, *J. Phys. B: At., Mol. Opt. Phys.* **1995**, *28*, 913.

169 J. S. Briggs, V. Schmidt, *J. Phys. B: At., Mol. Opt. Phys.* **2000**, *33*, R1.

170 J. A. R. Samson, *Phys. Rev. Lett.* **1990**, *65*, 2861.

171 A. Knapp, A. Kheifets, I. Bray, T. Weber, A. L. Landers, S. Schössler, T. Jahnke, J. Nickles, S. Kammer, O. Jagutzki, L. P. H. Schmidt, T. Osipov, J. Rösch, M. H. Prior, H. Schmidt-Böcking, C. L. Cocke, R. Dörner, *Phys. Rev. Lett.* **2002**, *89*, 033004.

172 C. A. Coulson, *Math. Proc. Cambridge Philos. Soc.* **1941**, *37*, 55.

173 I. R. Epstein, A. C. Tanner, in *Compton Scattering*, ed. by B. G. Williams, McGraw-Hill, New York, **1977**, pp. 209–233.

174 T. Koga, M. Morita, *Theor. Chim. Acta* **1982**, *61*, 73.

175 A. Dorn, A. Elliott, J. Lower, E. Weigold, J. Berakdar, A. Engelns, H. Klar, *Phys. Rev. Lett.* **1998**, *80*, 257.

176 R. N. Zare, *Mol. Photochem.* **1972**, *4*, 1.

177 E. Shigemasa, J. Adachi, M. Oura, A. Yagishita, *Phys. Rev. Lett.* **1995**, *74*, 359.

178 M. Takahashi, J. P. Cave, J. H. D. Eland, *Rev. Sci. Instrum.* **2000**, *71*, 1337.

179 M. Takahashi, N. Watanabe, Y. Khajuria, K. Nakayama, Y. Udagawa, J. H. D. Eland, *J. Electron Spectrosc. Relat. Phenom.* **2004**, *141*, 83.

180 M. Takahashi, N. Watanabe, Y. Khajuria, Y. Udagawa, J. H. D. Eland, *Phys. Rev. Lett.* **2005**, *94*, 213202.

181 K. Ito, J. Adachi, R. Hall, S. Motoki, E. Shigemasa, K. Soejima, A. Yagishita, *J. Phys. B: At., Mol. Opt. Phys.* **2000**, *33*, 527.

182 Y. Hikosaka, J. H. D. Eland, *Chem. Phys.* **2002**, *277*, 53.

183 A. K. Edwards, R. M. Wood, J. L. Davis, R. L. Ezell, *Phys. Rev. A* **1990**, *42*, 1367.

184 K. Ito, R. I. Hall, M. Ukai, *J. Chem. Phys.* **1996**, *104*, 8449.

185 G. H. Dunn, *Phys. Rev. Lett.* **1962**, *8*, 62.

186 M. Shibuya, Y. Asano, N. Watanabe, M. Takahashi, to be submitted.

187 M. Takahashi, Y. Udagawa, in *Nanoscale Interactions and Their Applications: Essays in Honour of Ian McCarthy*, ed. by F. Wang, M. J. Brunger, Transworld Research Network, Kerala, **2007**, pp. 157–168.

188 J. Rolke, Y. Zheng, C. E. Brion, Z. Shi, S. Wolfe, E. R. Davidson, *Chem. Phys.* **1999**, *244*, 1.

189 J. Rolke, Y. Zheng, C. E. Brion, S. J. Chakravorty, E. R. Davidson, I. E. McCarthy, *Chem. Phys.* **1997**, *215*, 191.

190 H. R. J. Walters, *Phys. Rep.* **1984**, *116*, 1.

191 T. Suzuki, *Annu. Rev. Phys. Chem.* **2006**, *57*, 555.

192 B. J. Siwick, J. R. Dwyer, R. E. Jordan, R. J. D. Miller, *Science* **2003**, *302*, 1382.

193 J. Itatani, J. Levesque, D. Zeidler, H. Niikura, H. Pépin, J. C. Kieffer, P. B. Corkum, D. M. Villeneuve, *Nature* **2004**, *432*, 867.

Masahiko Takahashi was born in Nagasaki in 1963 and brought up in Osaka. He got a B.Sc. degree in 1985 from Kyoto University. In the very last part of the M.Sc. program in Kyoto University, he became a technical associate in the Institute for Molecular Science (IMS) in Okazaki. Afterwards he became a research associate and got a Ph.D. from Kyoto University in 1992. Then he moved to the Research Institute for Scientific Measurements at Tohoku University and was promoted to an associate professor in 1999. During this term, he spent one year at Oxford University as a postdoctoral fellow. As well, he had an opportunity to work at IMS as a visiting associate professor for two years starting from 2003. In 2008 he was promoted to a full professor in the Institute of Multidisciplinary Research for Advanced Materials at Tohoku University. His current interest focuses on application of electron Compton scattering to a wide range of fields including not only atomic & molecular physics but also material technology and life science. He received the Award of the Association for Scientific Measurements for 2006 and The Chemical Society of Japan Award for Creative Work for 2007.